# ITRF/LhARA milestone M2.1 report

## *Baseline simulations of the future LhARA proton and ion source*

**Work Package 1.2**

T.S. Dascalu[1], E. Boella[1,2], N.P. Dover[3], R.J. Gray[2,4]

[1] *Department of Physics, Lancaster University, Bailrigg, Lancaster LA1 4YW, UK*
[2] *Cockcroft Institute, Daresbury Laboratory, Sci-Tech Daresbury, Keckwick Ln, Daresbury, Warrington UK*
[3] *John Adams Institute for Accelerator Science, Imperial College London, London SW7 2AZ, UK*
[4] *Department of Physics, SUPA, University of Strathclyde, John Anderson Building, 107 Rottenrow East, Glasgow G4 0NG, UK*

## Abstract

Here we present the results of a simulation campaign to support the development of the LhARA ion source. After a brief review of the ion source physics, we describe the different simulation methods we have used. We then present results of various optimisation studies to develop a baseline which will motivate and inform upcoming experimental studies. Although most of the current work is focused on protons, we will also provide an outlook on heavier ion (e.g. carbon) performance.

## Contents

# 1 Introduction

The objective of this milestone report is to summarise progress in the simulation campaign to inform the major baseline parameters of the proton and ion source envisioned for LhARA. Hydrodynamic and kinetic (2-D parameter scans and full 3-D Particle-In-Cell) simulations have been set up, run, and analysed to establish the baseline proton and ion production rates, energy spectra, and spatial distributions of the protons and ions generated by the LhARA source. We report a prediction of a set of optimised laser and target parameters for 300+ TW laser systems.

Several baseline requirements for the LhARA proton and ion source have been identified [1] to ensure that the LhARA facility can deliver beams suitable for the radiobiology programme envisioned by the collaboration. The most important baseline requirements from the LhARA source are:

- proton energies of $15\,\mathrm{MeV}$ and potentially above,
- different ion types e.g. $C^{6+}$ up to $4\,\mathrm{MeV/u}$,
- high single shot particle flux: e.g. $10^9$ protons at $(15 \pm 2)$ MeV in a solid angle of 15 mSr,
- ultrashort pulse durations,
- $10\,\mathrm{Hz}$ operation,
- high stability both shot-to-shot and over long-term operation,
- coupling to the capture system.

Although WP1.2 is undertaking an experimental campaign to demonstrate these requirements, high-fidelity simulations of proton and ion generation are an essential tool for an initial evaluation of the beam characteristics achievable for the LhARA baseline conditions. In the context of simulations, the most important baseline requirements are the generation of $>15\,\mathrm{MeV}$ proton beams with tens of pico-Coulombs charge per bunch ($10^8$–$10^9$ protons) and minimal beam divergence at the source. We accounted indirectly for the other requirements by limiting the parameter space that we explored within the limits of well-established technology for the laser and the targetry systems.

The first goal of the campaign of simulations that we present in this report was to identify the laser and target parameters which ensure that the baseline requirements of the source are satisfied. A second objective of the simulations was to explore the wide parameter space to find the optimal source parameters that could potentially push the beam characteristics well above the baseline requirements. We used laser pulse specifications similar to the ones available at SCAPA [2] where experiments are underway to characterise the proton and ion source at near the final ITRF/LhARA specifications.

## 1.1 Overview of Target Normal Sheath Acceleration (TNSA)

Given its robustness, target normal sheath acceleration (TNSA) is the most widely investigated ion acceleration mechanism based on laser-plasma interactions. TNSA is currently the preferred mechanism for developing applications using relatively low-energy-laser-driven ion sources at high repetition rates. However, the main limitation of TNSA lies in the current limits on the maximum achievable ion energies. The maximum energies recorded so far have been attained using Petawatt laser systems operating at low repetition rates.

The fundamental features of the TNSA process are illustrated in Figure. 1. Thin foils ranging from a few hundred nanometres to tens of micrometres in thickness are irradiated by an intense laser pulse, operating within an intensity regime defined by the guideline $I_0\lambda_0^2 > 10^{18}\,\mathrm{W/cm^2\mu m^2}$, where $I_0$ represents the laser intensity and $\lambda_0$ denotes the wavelength. Initially, the leading edge of the laser pulse interacts with the front surface of the target, forming a ‘preplasma’. Subsequently the peak of the pulse is absorbed depending on the preplasma properties, converting a large percentage of its energy to electrons. These hot electrons’ total number

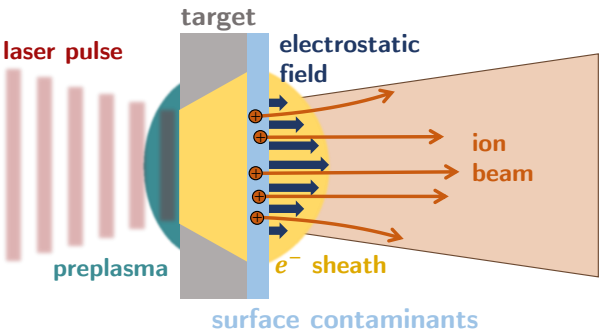


Figure 1: Schematic diagram of target normal sheath acceleration (TNSA) from an intense laser impinging on a solid target. Hot electrons from the preplasma form a strong electrostatic sheath field at the target's rear, which accelerates the ions from the target surface into the vacuum. Typical surface contaminants are hydrocarbons and water vapour. Figure reproduced from [3].

and temperature significantly influence the overall acceleration achievable through TNSA. These electrons have energies on the order of MeV, enabling them to propagate into the bulk of the target towards the rear surface.

While a limited number of sufficiently energetic electrons exit the target, the majority are retained by the positive space-charge forming within the target. These high-energy electrons circulate between the front and rear surfaces, generating an electron sheath on both sides that extends beyond the initially unperturbed surfaces of the target. Consequently, this sheath establishes a powerful accelerating electric field well in excess of 10 TV per meter [4], a million times higher than that used in conventional accelerators. This field contributes to ionising surface ions and accelerates ions out of the foil at high speeds.

The strength of the sheath fields typically increases with higher electron temperatures, leading to enhanced maximum ion energies. Similarly, an improvement in ion energy can result from the recirculation of hot electrons through the target during the acceleration process, provided the target thickness and pulse duration are appropriately matched [5]. TNSA accelerating ions at the front target surface is less efficient due to the presence of the preplasma.

In principle, TNSA can accelerate any ion species present in the surface layers of the target. However, in many experiments, TNSA tends to preferentially accelerate light ions such as protons, carbon, and oxygen ions originating from contaminant layers rather than ions from the bulk of the target material. Protons are particularly favoured due to their high charge-to-mass ratio, resulting in their acceleration first which then screens the accelerating field experienced by the heavier ion species. Consequently, to preferentially accelerate ion species heavier than protons from the material of the target itself, contaminants on the target surface must be removed prior to laser irradiation.

### Ion energy spectrum

The proton and ion beams generated through the interaction of a high-intensity laser with a solid target exhibit a characteristic broad energy spectrum, extending up to tens of MeV (see, for instance, references [6–9]). Both protons and heavier ions are accelerated from water vapour or hydrocarbon contamination invariably present on the target surface due to the inherent challenges in achieving perfect vacuum conditions. In addition to their broad energy distribution, proton and ion beams generated by laser-driven sources via TNSA are typically characterised by large opening angles at the source. Reports indicate full beam-envelope opening angles of several tens of degrees for proton beams [10]. Generally, this angle decreases as proton energy increases [11].

Several laser and target parameters play crucial roles in determining the resulting particle energy spectrum. For proton acceleration using the TNSA scheme, some of the parameters empirically identified to influence the

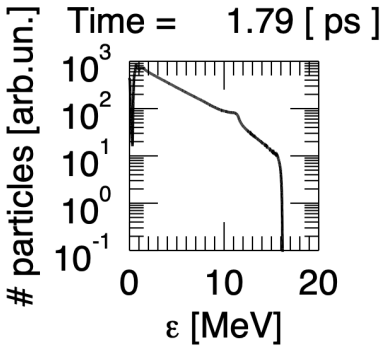


Figure 2: Example of a typical energy spectrum for protons and ions produced via the TNSA mechanism. The particle number decreases with an increase in the kinetic energy, $\epsilon$, according to a pseudo-thermal spectrum up to a maximum cutoff energy where the spectrum exhibits a sharp drop. The spectrum was extracted from a 3-D PIC simulation. The local increase in the particle flux around $11\,\mathrm{MeV}$ is unphysical and typically vanishes as the particles propagate away from the target.

energy spectrum include the target material [12], target thickness [5], laser intensity and pulse energy [13], and the presence of a preplasma [14].

The typical energy spectrum of ions produced via TNSA exhibits a broad distribution spanning from low to high energies. This spectrum is characterised by its continuous nature with an exponential pseudo-thermal part where the particle flux decreases from the lower to the higher energies and a sharp drop in the flux near the maximum ion energy achieved during the acceleration. The energy spectrum reflects the diverse acceleration mechanisms at play within the plasma generated by the interaction of an intense laser pulse with a solid target. An example of a typical energy spectrum is shown in Figure 2 for the case of proton acceleration as obtained in a 3-D PIC simulation. For heavier ions generated by laser-plasma acceleration, the energy spectrum shows the same exponential decrease as in the case of protons [15].

The energy of the accelerated ions is not confined to discrete values but instead covers a broad range due to several factors. Firstly, ions are accelerated from different depths within the target material, resulting in a range of energies depending on their initial positions relative to the target surface. Secondly, the strength of the electrostatic fields at the target rear surface varies spatially, leading to ions experiencing different levels of acceleration depending on their trajectories within the plasma [16]. Finally, hydrocarbon contamination or residual gases present on the target surface can contribute to the ion acceleration process, introducing additional complexity to the energy spectrum.

In this report, we use the term ‘cutoff energy’ to refer to the maximum energy attained by protons or ions within the TNSA energy spectrum. It represents the maximum proton or ion energy produced by the acceleration mechanism. The cutoff energy is often defined as the energy at which the ion spectrum begins to exhibit a significant decrease in intensity or falls below a certain threshold value. As in experimental studies, the cutoff energy serves as a critical parameter for characterising the efficiency and effectiveness of TNSA-driven ion acceleration, we also use it in this report as a main figure of merit. Understanding and controlling the cutoff energy are essential for optimising TNSA-based applications and, thus, are relevant for the development of the LhARA ion source.

Table 1: Important free parameters that are known to play a role in the acceleration of protons and ions via TNSA.

| | Parameter | References |
|---|---|---|
| Laser | Laser energy | [17, 18] |
| | Focal spot size | [17–19] |
| | Pulse length | [17] |
| | Angle of incidence | [9] |
| | Spectral phase | [20] |
| Target | Thickness | [5, 21] |
| | Preplasma formation and scale-length | [14, 16, 22–24] |
| | Ion species of surface contaminants | [25, 26] |
| | Lateral size | [27] |

**Free parameters that impact proton and ion acceleration**

There are several parameters linked to the laser pulse and the target that were previously shown in both simulations and experiments to play a role in the acceleration of protons and ions via TNSA. In our programme of simulations, we investigated the subset of parameters which can be well controlled in an experimental setting and which are known to significantly impact one of the stages of the TNSA mechanism. For example, we scanned those parameters that play a role in the energy transfer from the laser pulse to the hot electrons or the strength of the accelerating sheath generated by the hot electrons on the back of the target. Table 1 lists some of the main parameters of interest for optimising the LhARA source together with a few representative references of the impact on the beam production which was previously reported for each parameter.

## 2 Hydrodynamic modelling of laser contrast

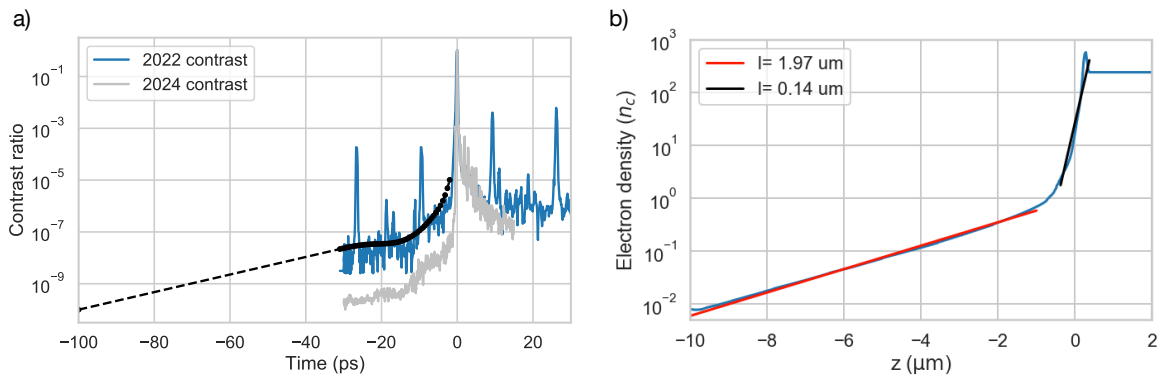


Figure 3: a) The laser contrast curve for the SCAPA laser measured in 2022 (blue), and input to FLASH code (dashed black). The larger prepulses near $-10$ and $-28\,\mathrm{ps}$ are measurement artefacts. An updated contrast curve taken in May 2024 (grey) shows improvements to the contrast, which will be incorporated into the modelling soon. b) Predicted axial density profile on the front surface of the target. A typical double exponential scale is shown to form during the prepulse-driven ablation. The initial target front surface was at $z = 0\,\mu\mathrm{m}$.

A well-known feature of laser-driven ion sources is sensitivity to the laser prepulse, which here refers to any laser energy arriving at the target before the high energy, high-intensity main pulse. This is typically characterised by the laser contrast, as shown in Figure 3a for the SCAPA laser system. The laser contrast curve plotted in Figure 3a represents an early measurement carried out on SCAPA which was available at the time of running the hydrodynamic simulations described in this section. Subsequently, additional measurements have been carried out and the contrast profile has been improved considerably. In Figure 3a, the longer time scale amplified spontaneous emission (ASE) is not shown, but will extend at a lower intensity up to a nanosecond. Future modelling will also take this into account.

Although modern laser systems utilise numerous advanced techniques to minimise the contrast [28], the wavelength-scale focal spot typically results in significant target ionisation and heating picoseconds to nanoseconds before the main pulse. This results in ablation of the front surface, causing a shockwave to be driven into the target and a plasma plume to be ejected away from the target. When the high-intensity main pulse arrives, it has to travel through the plasma plume up to the dense part of the target, and therefore the properties of the plasma plume, or so-called pre-plasma, can often dominate the laser absorption properties, and therefore also the characteristics of the ensuing laser-driven ion source.

Simulating the laser prepulse is, therefore, an important part of the modelling stack, and can be used to determine the initial conditions of Particle-in-Cell simulations of the high-intensity pulse interaction. Therefore, the FLASH code [29] has been used to estimate the influence of the laser prepulse. This code has been widely used in the high energy density physics community for this application. The code was run in 2D cylindrical geometry and models the prepulse absorption with an inverse bremsstrahlung heating model based on ray tracing. Heat conduction and exchange between electrons and ions are based on the Lee-More model. An example density profile at the centre of the laser axis for the SCAPA laser contrast is shown in Figure. 3b. The laser contrast can vary on laser amplification parameters, and the effect on the density profile will also depend on irradiation conditions, including focal size and target material type. The simulation model presented here can easily be extended to different irradiation or target conditions. Although the simulations are currently performed in 2D-cylindrical geometry, the FLASH code has the capability to be extended to be fully 3D to properly model off-normal angle of incidence laser pulses if required.

As a general property, the prepulse-driven ablation plasma has two scale lengths. This is due to the heating characteristics of the laser. The heating rate for inverse bremsstrahlung increases exponentially as the ionised electron density reaches the plasma critical density. Therefore, most of the absorption happens in a relatively confined region around the plasma critical density. The longer scale length, highlighted in red in Figure 3b, is the ablation plasma. This is matter that has been driven away from the front surface due to the thermal pressure generated at the critical density surface. The shorter scale length, indicated in black, is the conduction layer. Here, plasma heating is dominated by heat conduction into the target from the critical density surface. Additionally, collisional shockwaves can also be generated and driven into the target. These generate density perturbations, but as they propagate in dense bulk they are normally considered to only impact the ion source if they are fast enough to break out the rear side of the target. If this happens, the rapid expansion of the rear surface will negatively impact TNSA driven by the later main laser pulse. This typically imposes a minimum usable target thickness for a particular laser system.

## 3 The Particle-In-Cell (PIC) technique

The underpinning interaction between the main laser pulse and a plasma is intrinsically non-linear, multi-dimensional, and can be properly simulated only through the kinetic approach. Among the different possibilities, Particle-In-Cell (PIC) codes [30] represent perhaps the most suitable choice in this case due to the reduced number of physical approximations and their ability to take full advantage of High-Performance Computing

(HPC) resources.

## 3.1 Outline of the PIC method

PIC codes offer a means to simulate the collective behaviour of a plasma by tracking the dynamics of an ensemble of macro-particles, each representing a discrete portion of the continuous distribution function in phase-space. Essentially, these macro-particles can be conceptualised as a cloud of numerous real particles or as elements of an incompressible fluid moving within a six-dimensional phase-space. Each macro-particle possesses attributes such as charge ($q$) and mass ($m$), determined by the number of real particles it represents while maintaining the $q/m$ ratio of the actual plasma species.

Furthermore, macro-particles are characterised by finite size. While the PIC method is adept at capturing the collective behaviour dictated by the long-range Coulomb interactions between particles, the abrupt changes in forces during close encounters can lead to undesirable collisional effects in a collisionless model. To mitigate this issue, finite-sized macro-particles are employed, wherein the charge of each particle is distributed over a finite region of space, typically across multiple grid cells via a particle shape function. Consequently, variations in charge density smaller than the size of a cell or macro-particle cannot be resolved in a PIC simulation. Hence, realistic PIC simulations must use suitably small grid cells in order to avoid the appearance of numerical heating and unphysical effects.

PIC models are extensively used to simulate the interaction between lasers and plasmas due to their ability to capture the complex dynamics of both the electromagnetic fields and the charged particles within the plasma. Various numerical techniques have been developed to simulate kinetic processes within a plasma. The investigations outlined in this report rely on the particle-in-cell (PIC) method implemented through the OSIRIS code (version 4.4).

OSIRIS is a multidimensional, massively parallel, fully relativistic PIC code [31]. The code is written in Fortran 90 using the object-oriented paradigm. It is parallelised using MPI and OpenMP. Data input and output are very efficiently executed through the utilisation of the Hierarchical Data Format (HDF5) file format. OSIRIS contains algorithms for one-, two- and three-dimensional simulations in Cartesian coordinates and for two-dimensional simulations in azimuthally symmetric cylindrical coordinates. OSIRIS' massively parallelised algorithm has been optimised to take full advantage of the largest HPC systems. The work summarised in this report has been carried out on two HPC systems: ARCHER2 (EPCC, UK) [32] and SuperMUC-NG (LRZ, Germany) [33], with most of the simulations using up to 12,288 cores in parallel.

For the majority of the results presented in this report, we explored the impact of several laser and target parameters by using Particle-In-Cell (PIC) simulations. Due to the comparatively large computation resources required by full-scale 3-D simulations, we also made use of 2-D simulations which allowed us to investigate larger parameter spaces. We stress that, as it is well known [34–36], 2-D simulations overestimate the final ion energy due to the logarithmic growth in time of the proton cutoff energy. Nonetheless, 2-D numerical simulations still offer a valid insight into the underpinning physics [34].

## 3.2 Convergence testing and bench-marking

A series of high-fidelity PIC simulations were carried out prior to the work highlighted in this report to explore the impact of varying several parameters typical to PIC simulations on the characteristics of the protons accelerated via TNSA from a solid target. Comprehensive parameter scans were performed with the use of the OSIRIS framework and the ARCHER2 computing cluster. A description of the simulations and the resulting conclusions can be found in [37]. Here, we briefly summarise the main findings based on which we chose the main set of parameters for the realistic PIC simulations presented in the rest of this report.

Firstly, the initial electron temperature and the ionisation level of the material of the target were found to have a marginal effect on the characteristics of the protons accelerated by TNSA. These two variables cannot be effectively controlled in an experimental setup. However, although the laser prepulse pre-heats and ionises the front of the target, the low energy in the prepulse means that it is negligible compared to the main pulse. Indeed, the simulations showed that no significant changes were observed in the electron heating efficiency or the resulting proton spectrum when either the initial electron temperature or ionisation level of the target ions was varied in simulations.

Secondly, the protons that are accelerated via TNSA originate from a layer of contaminants on the back of the target that contains hydrogen atoms. It was found previously [37] that thinner contaminant layers result in ion-accelerating fields with similar strengths which, however, decay slower than in the presence of thicker hydrogen layers. As a result, using thinner contaminant layers leads to higher proton cutoff energies. In the simulations presented in this report, we considered the contaminant ion species to form a layer with a thickness of $31.8\,\mathrm{nm}$ on the back of the target in which case the minimum thickness was limited only by the resolution of the spatial grid. The thickness of the contaminant layer has not been well studied experimentally so far and, thus, there is limited data to guide the modelling of target's rear surface in simulations.

Furthermore, the number of macro-particles per cell and the resolution of the spatial grid were both chosen based on previous convergence tests. The OSIRIS code used an algorithm that conserves momentum, but not energy. Therefore, the degree to which the total energy of the system changes in a simulation can be affected by the resolution of the spatial grid. At the same time, decreasing the grid size rapidly makes a simulation increasingly more computationally expensive as the grid resolution also dictates the time step that is possible to use. The particular set of parameters we used in the PIC simulations to model the TNSA regime from a solid target is provided in the next section.

# 4 Modelling of TNSA for proton acceleration on SCAPA

## 4.1 Overview of the computational model

The model we set up for the acceleration of protons from a solid target by TNSA is based on the general (baseline) set of parameters summarised in Table 2. In the following parameter scans, the baseline parameters were kept constant with the exception of the tested variable to study its impact on the acceleration of protons. A brief description of the model is given in the following paragraph.

The PIC simulations we have conducted explored the interaction of the SCAPA Ti:sapphire laser (laser wavelength $\lambda_0 = 800\,\mathrm{nm}$) with aluminium foils $6\,\mu\mathrm{m}$ thick. Due to the constraints of the tape drive system used at SCAPA, the experiments have been carried out so far with targets with a thickness in the range $10$–$15\,\mu\mathrm{m}$ made of denser materials like steel or copper. This is likely to reduce the maximum achievable proton energy in experiments compared to the predictions from the simulations reported here.

In addition to the tape-like target, we considered a baseline full laser energy on target of $3.75\,\mathrm{J}$ out of which a fraction of $25\,\%$ is contained within the laser spot. We must note that the baseline laser energy chosen for the majority of simulations represents a conservative fraction of the laser energy typically employed in experiments at SCAPA [2] ($\sim$6.6 J). Nonetheless, we explored higher pulse energies and higher laser intensities compared to the baseline case in dedicated parameter scans. Considering the baseline laser energy, we performed simulations with a laser intensity of $9.97\times10^{20}\,\mathrm{W/cm^2}$ for normalised vector potential $a_0 = 21.60$. The p-polarised pulses were focused on the target to a spot size $w_0$ of $1.5\,\mu\mathrm{m}$ and had a FWHM pulse duration of $25\,\mathrm{fs}$.

The target was modelled as a pre-formed plasma composed of $Al^{3+}$ ions and electrons with density $70\,n_c \sim 10^{23}\,\mathrm{cm^{-3}}$ (here $n_c$ is the critical density corresponding to the laser frequency). On the back of the target, a thin layer of $H^+$ ions was inserted to mimic contaminants naturally present on the back surface of solid targets.

Table 2: Summary table of the main parameters used to model the TNSA mechanism for proton acceleration under similar conditions to the experiments at SCAPA [2].

| | **Parameter** | **Value** | **Unit** |
|---|---|---|---|
| Laser | Energy (in the laser spot) | 0.938 | J |
| (p-polarised) | Pulse duration | 25 | fs |
| | Power | 35.24 | TW |
| | Intensity ($I_0$) | $9.97 \times 10^{20}$ | $\mathrm{W/cm^3}$ |
| | Spot size$^\dagger$ ($w_0$) | 1.5 | µm |
| | Laser pulse rise/fall time | 25.06 | fs |
| | Wavelength ($\lambda_0$) | 800 | nm |
| | Norm. laser vector potential ($a_0$) | 21.60 | |
| | Critical density ($n_c$) | $1.74 \times 10^{21}$ | $1/\mathrm{cm^3}$ |
| Target | Thickness | 6 | µm |
| ($Al^{3+}$) | Density | 70 | $n_c$ |
| | $H^+$ layer thickness | 31.83 | nm |
| | $H^+$ layer density | 1.15 | $n_c$ |
| | Initial particle temperature | 10 | keV |

$^\dagger w_0$ is the pulse waist ($= \mathrm{FWHM}/\sqrt{2\ln 2}$)

If not mentioned otherwise, the simulations described in each of the following sections modelled the normal incidence of the laser onto the solid target.

The longitudinal profile of the laser was modelled as a Gaussian-like 5-th order polynomial profile with a rise and fall time of $59/\omega_0$ (see the reference guide of OSIRIS [38]). The time the laser pulse holds its peak value was set to zero. The laser was focused on the front surface of the bulk of the target (excluding the preplasma region). All particle species inside the target were initialised according to an isotropic thermal momentum distribution based on an initial temperature. For the full 3-D simulations, the number of macro-particles per cell was 2, 8, and 27 for the aluminium, electron, and hydrogen species, respectively. Absorbing periodic boundaries were used in most of the simulations for particle species and perfectly matched layers were employed as absorbing boundary conditions for the electromagnetic fields.

The size of the simulation domain was dictated by two factors. Firstly, the domain was chosen for each simulation to be large enough for the accelerated protons not to leave the simulation box earlier than the end of the simulation. Secondly, the transverse size of the domain was always at least ten times the laser spot size. The size of a cell of the computational grid was fixed to $dx = dy = dz = \frac{1}{8}\,(c/\omega_0)$ as required as a result of the convergence studies. A typical simulation with the laser at normal incidence on the target contained $8784\times944\times944$ cells in the spatial grid. Larger simulation domains were used in the case of oblique laser incidence. The choice of the magnitude of the time step is severely constrained by the fields discretisation scheme and is, thus, fully determined from the spatial resolution of the grid.

**Models of the preplasma**

To explore the presence of a preplasma, the front of the target was modelled using two techniques. Initially,

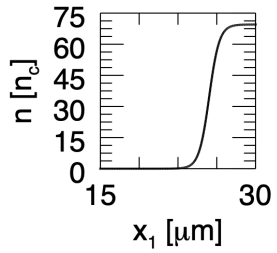


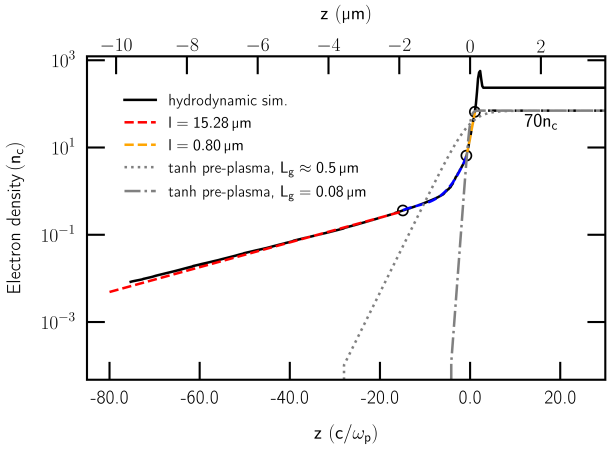


Figure 4: Left: An example of an idealised preplasma profile modelled as a hyperbolic tangent function (see eq. 1). The front surface of the unperturbed target is located at $25.5\,\mu\mathrm{m}$. Right: Predicted axial density profile on the front surface of the target from the hydrodynamic simulation compared to the idealised tanh model for a couple of scale-lengths $L_g$. A typical double exponential scale is shown to form during the prepulse-driven ablation.

an idealised density profile was considered based on the hyperbolic tangent function with the parameter $L_g$ determining the preplasma scale-length. The pre-expanded plasma in front of the target was modelled using the function

$$n_{Al^{3+}} = 70\frac{n_c}{2}\left[\tanh\left(\frac{x_1 - x_{1,0}}{L_g}\right) + 1\right], \tag{1}$$

where $x_1$ is the longitudinal coordinate, $x_{1,0} = 25.5\,\mu\mathrm{m}$, and the preplasma scale lengths we investigated are within the range $0.08$–$1\,\mu\mathrm{m}$.

Once the first set of measurements of the laser contrast at SCAPA was available, hydrodynamic simulations were carried out to extract a more realistic preplasma density profile, as described in section 2. The laser intensity contrast is the ratio of the peak laser intensity to the intensity of the light that precedes it. The target density profile obtained from the hydrodynamic simulations was used as an input to the PIC simulations to define the spatial distribution of the particle species at the beginning of the simulations. Figure 4 shows an example of preplasma density profile calculated with the hyperbolic tangent function in comparison to the more realistic density curve extracted from a hydrodynamic simulation.

## 4.2 Impact of laser parameters

**Laser intensity (varying pulse energy)**

The parameter scan over laser intensity was performed considering a $6\,\mu\mathrm{m}$ thick aluminium target and optimal laser contrast. Laser intensities in the range $(8$–$10) \times 10^{20}\,\mathrm{W/cm^2}$, corresponding to normalised vector potentials $a_0 = 19.32$–$21.60$, were considered. The p-polarised pulses were focused on the target to a spot size of $1.5\,\mu\mathrm{m}$ and had a duration at FWHM of $25\,\mathrm{fs}$. The intensity of the laser was varied by changing the energy of the pulse, while the laser spot size was kept constant.

These 3-D PIC simulations suggest that, under these conditions, a more powerful laser must be considered for LhARA. In particular, since the proton cutoff energy scales linearly with the laser intensity, to extend the proton spectrum beyond $20\,\mathrm{MeV}$ and accelerate sufficient protons to energies of $(15.0 \pm 0.5)\,\mathrm{MeV}$, requires laser intensities $\gg 10^{21}\,\mathrm{W/cm^2}$ (see Figure 5 which shows the proton cutoff energy versus laser intensity on

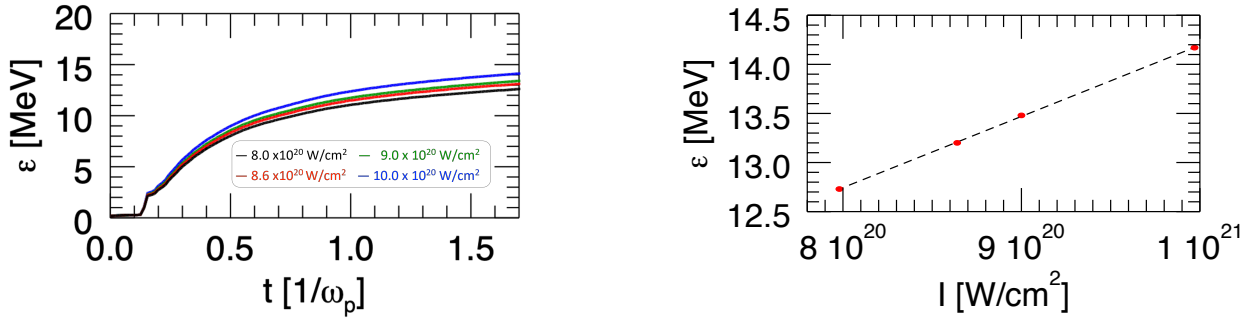


Figure 5: Evolution of the proton cutoff energy for different laser intensities (left panel): 8.0 (black), 8.6 (red), 9.0 (green), 10.0 (blue) ($\times 10^{20}$ W/cm$^2$). Proton cutoff energy at saturation vs laser intensity (right panel). The laser intensity was varied by changing the laser pulse energy while maintaining the focal spot size fixed. These simulations consider a 6 µm thick Al target and abrupt plasma-to-vacuum transition.

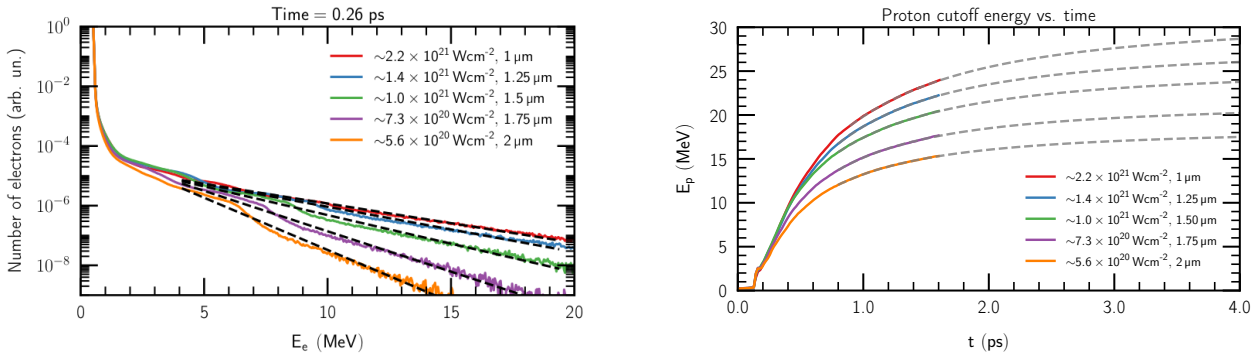


Figure 6: The energy spectrum of the electrons after the reflection of the laser pulse from the target (left panel). The hot electrons exhibit a pseudo-thermal distribution with higher temperatures for higher laser intensities. Evolution of the proton cutoff energy for different laser spot sizes at the focal plane (right panel). A model [39] was fitted to the data from simulations to infer the maximum proton energies at later times.

target). It is essential to evaluate carefully the laser temporal profile. A sub-optimal contrast with sufficiently thick targets could pre-expand the front surface of the target leading to preplasma formation but leaving the rear surface of the target intact. It is well known that the presence of a preplasma enables more efficient electron heating mechanisms. In turn, this translates into higher proton energies. We have also considered the possibility that a pre-pulse be used to generate the preplasma in front of the target in a more controlled way. Preliminary simulations modelling a pre-plasma in front of the target indicated that proton spectra extending beyond 20 MeV can be achieved with targets $> 2$ µm thick and laser intensities $\lesssim 10^{21}$ W/cm$^2$. Consequently, we performed simulations to optimise the preplasma scale length so as to attain LhARA goals in terms of proton energy and number.

**Laser intensity (varying focal spot size)**

In addition to increasing the energy per pulse, the laser intensity on the target can be increased by focusing the laser onto a smaller spot size. In principle, such an approach may have further benefits in decreasing the divergence of the proton beam since the transverse size of the accelerating sheath on the back of the target should also be reduced. This second parameter scan over laser intensity was performed considering a 6 µm thick aluminium target and a preplasma in front of the target modelled as a hyperbolic tangent density profile with scale-length $L_g = 0.5$ µm. We show in a following section that this idealised preplasma profile results in

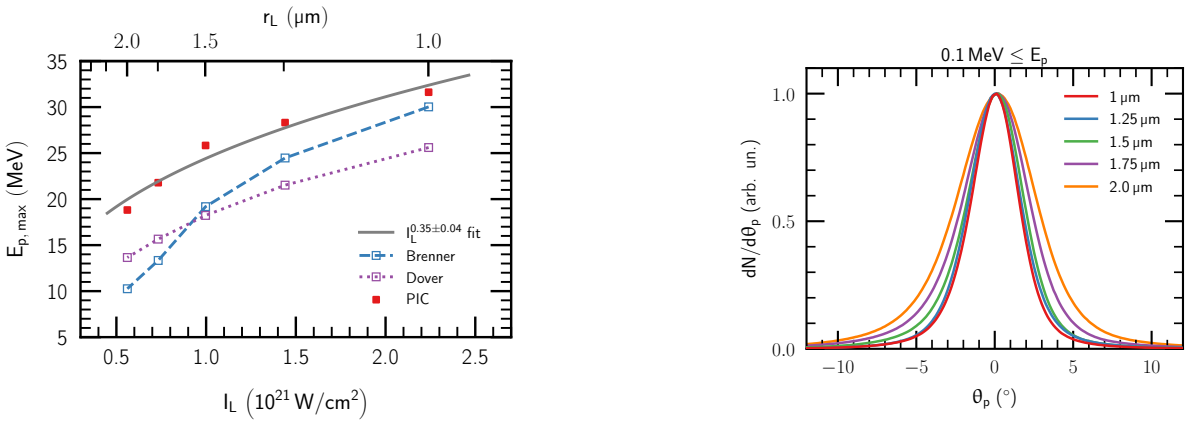


Figure 7: Proton cutoff energy at saturation vs laser intensity (left panel). The laser intensity was varied by changing the laser focal spot size at constant pulse energy. A power law fit is applied to the data from simulations. The predictions of two models (Brenner [40], Dover [19]) of TNSA are also shown. The angular distribution of protons that exit the target is measured with respect to the direction normal to the target (right panel). These simulations consider a 6 μm thick Al target and abrupt plasma-to-vacuum transition.

similar proton acceleration to the experimental conditions at SCAPA. The p-polarised laser pulse was focused on the front surface of the unperturbed target to a spot size, $w_0$, in the range 1.0–2.0 μm corresponding to laser intensities in the range $(5.61\text{–}22.4) \times 10^{20}\,\mathrm{W/cm^2}$ (normalised vector potential, $a_0$, in the range 16.2–32.4).

These 3-D PIC simulations suggest that, in the presence of a long-enough scale-length preplasma, laser intensities below $10^{21}\,\mathrm{W/cm^2}$ could reach proton cutoff energies $>15\,\mathrm{MeV}$ which are suitable for LhARA. However, to extend the proton spectrum beyond 20 MeV, even in the presence of the preplasma, the laser intensity must be at least $\sim 0.7 \times 10^{21}\,\mathrm{W/cm^2}$. This can be achieved with a spot size of 1.75 μm or smaller. Figure 6 shows that higher proton cutoff energies are obtained for smaller spot sizes, or equivalently higher laser intensities, as a result of the larger number of hot electrons that are accelerated by the laser pulse through the target at higher laser intensities. We used a theoretical model of the TNSA mechanism described in [39] to fit the time evolution of the cutoff energy from the simulations and obtain the saturation energy at a time significantly later than the interval of time captured by the simulations. The theoretical model is based on the calculation of the accelerating field created by a radially confined surface charge set up by laser-accelerated electrons on the target rear side.

We extracted the saturation energies inferred from the combination of the data from the simulations and the theoretical model and found a power-law dependence of the proton cutoff energy at saturation on either the laser spot size or intensity. The left panel of Figure 7 shows a comparison of the trend obtained from the simulations to a couple of well-known models from the literature [19, 40]. We notice that the simulations overestimate the proton cutoff energy in comparison to both models at the lower end of the intensity range. The trend from the simulations is, however, more similar to the predictions of [40] at the higher end of the intensity range that we explored. It must be mentioned that the predictions from both models require at least one free parameter that could not be directly extracted from the simulation data and, therefore, approximate values were used. Nonetheless, the theoretical models assume ideal laser contrast, while the simulations included a relatively long scale-length preplasma in front of the target. Thus, the cutoff energies predicted by the simulations are believed to be higher due to the more efficient energy transfer from the laser to hot electrons mediated by the presence of the preplasma.

In principle, the laser spot size could also contribute to the opening angle within which the protons are accelerated from the back of the target. The transverse size and shape of the electrostatic sheath created by the

hot electrons on the rear surface of the target are dictated mainly by the laser spot size and transverse intensity profile, and the material and thickness of the target. The PIC simulations revealed that irradiating the target using laser spots with smaller radii results in proton 'beams' with lower divergence, as shown by the right panel of Figure 7. Here, we define the divergence as the angle at which protons propagate away from the target measured with respect to the direction of incidence of the laser (or the normal to the target) in a spherical coordinate system ($z$-axis aligned with the laser propagation axis).

Even for the largest laser spot size that we explored, the protons are accelerated within a cone with a half-opening angle of $\sim 5^\circ$ or smaller. As a consequence, focusing the laser to a small spot size would bring a benefit to the LhARA proton source by reducing the overall divergence of the protons from the source. The final choice of the laser spot size requires a detailed evaluation of the opening angle of the cone within which the protons with the energies of interest for LhARA ($(15.0 \pm 0.5)\,\mathrm{MeV}$) propagate. This opening angle must be compared to the acceptance of the capture system planned for LhARA to decide whether the proton beam divergence at the source needs to be reduced. Nonetheless, if the laser system allows it, one way to reduce the proton beam divergence is by focusing the laser to a smaller spot size.

**Angle of incidence**

The mechanism by which energy is transferred from the laser pulse to the electrons in a micrometre-thick solid target is vastly dictated by the laser intensity [23, 41]. In addition, the polarisation of the laser [21, 42] and its direction of incidence with respect to the target [9, 43] also play an important role in the effectiveness of the energy transfer from the laser to the electrons and, hence, to the ions accelerated in the TNSA regime. 3-D PIC simulations [43] show that under specific conditions there is an optimum incidence angle at which the ion energies can be significantly greater than those achieved at normal incidence. The existence of an optimum angle is a result of the interplay between two counteracting effects. On the one hand, a larger fraction of the laser energy is absorbed by the electrons in the target at oblique incidence. On the other hand, the hot electrons are pushed more efficiently out of the target and form a stronger ion-accelerating sheath at normal incidence. In other words, the hot electrons propagate through more material of the target as the angle of incidence increases (see Figure 8) and they lose more energy before establishing the accelerating sheath at the back of the target.

To predict the optimal incidence angle of the laser under conditions similar to the experiments at SCAPA, we conducted a set of 2-D PIC simulations. We considered a $6\,\mu\mathrm{m}$-thick Al target and a laser intensity $I_0 = 9.97 \times 10^{20}\,\mathrm{W/cm^2}$. The model included the preplasma density profile obtained from a hydrodynamic simulation of the laser prepulse interacting with the target starting from a preliminary measurement of the laser contrast curve at SCAPA. The laser was considered to have p-polarisation.

The version of the OSIRIS code that was used for the PIC simulations described in this report requires the laser pulse to be injected in the simulation domain perpendicularly from one of the boundaries of the simulation. Thus, the target has to be rotated with respect to the boundary from where the laser pulse is injected in order to model oblique incidence of the laser onto the target (see Figure 8). As a result, the simulation domain needs to be larger along one of the transverse directions and along the longitudinal axis by comparison with the case of normal incidence. This is a consequence of the ions being accelerated normal to the target at an oblique angle with respect to the longitudinal axis of the simulation (i.e. the laser propagation axis). Under these conditions, the simulation domain needs to be enlarged to avoid the fastest ions exiting the domain before the acceleration process has reached the point of energy saturation. Ultimately, rotating the target by large angles with respect to the propagation axis of the laser increases the computational resources required to simulate in three dimensions the acceleration of protons up to the point of energy saturation. The computational requirements become more manageable in the case of using 2-D PIC simulations.

A scan of the incidence angle of the laser was performed starting at normal incidence and up to an angle of $60^\circ$. Figure 9 indicates that there is an optimal incidence angle near approximately $28^\circ$ that results in a

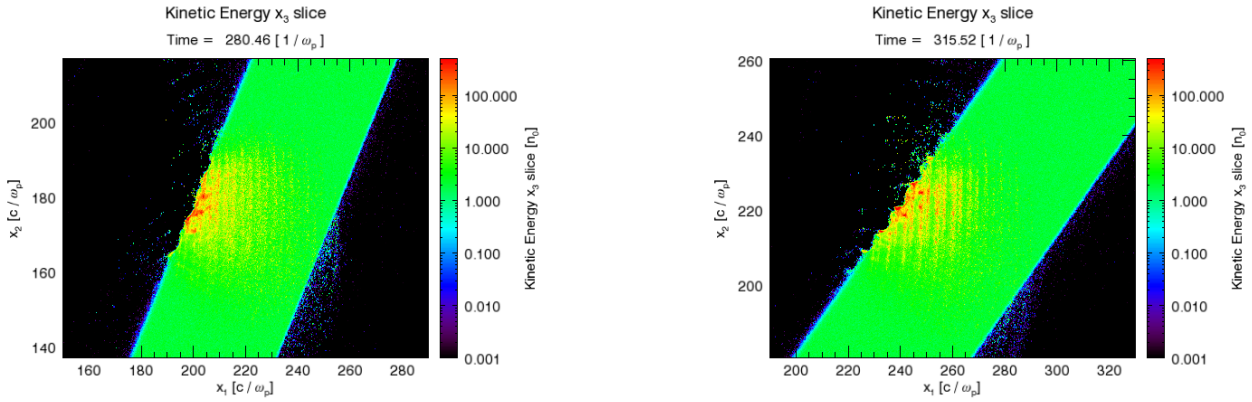


Figure 8: The density of kinetic energy carried by electrons in a transverse slice through the oblique target along the mid-plane of a 3-D PIC simulation for laser incidence at $30°$ (left) and $45°$ (right). The laser has hit the front surface of the target propagating horizontally from the left boundary of each diagram to its right boundary.

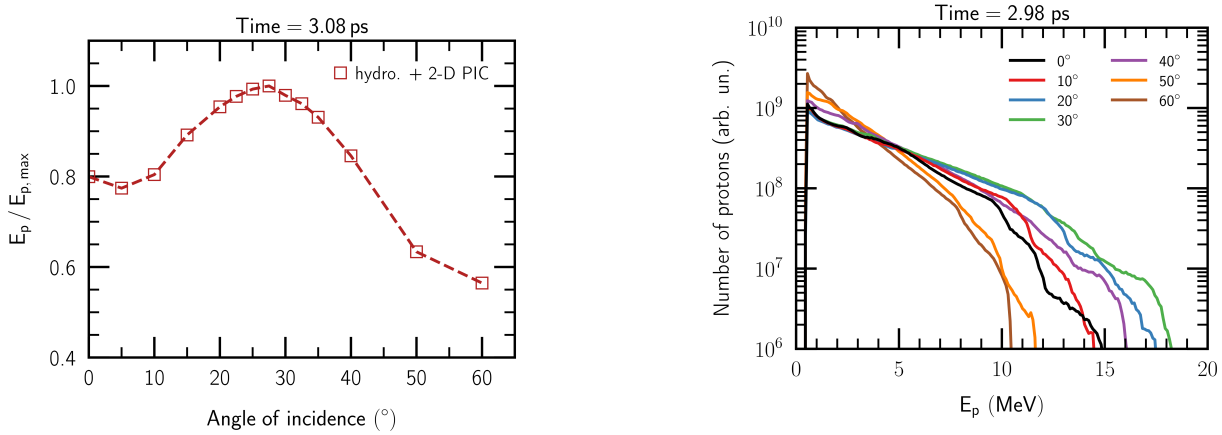


Figure 9: Proton cutoff energy at saturation (approximately $3\,\mathrm{ps}$ after the laser hits the front surface of the target) vs the angle of incidence of the laser on the solid target (left panel). The cutoff energies are normalised with respect to the maximum value found at approximately $27.5°$. Proton energy spectra at saturation for a series of incidence angles of the laser onto the target (right panel). These simulations consider a $6\,\mu\mathrm{m}$-thick Al target with a preplasma density profile obtained from a hydrodynamic simulation using a preliminary laser contrast curve measured at SCAPA. The laser intensity is $I_0 = 9.97 \times 10^{20}\,\mathrm{W/cm^2}$.

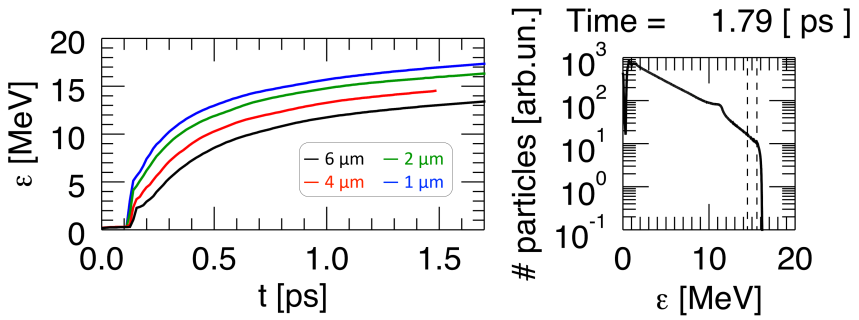


Figure 10: Evolution of the proton cutoff energy for different target thicknesses (left panel). Proton energy spectrum at saturation for a $2\,\mu\mathrm{m}$ thick Al target (right panel). The dashed lines indicate the range of energies of interest. These simulations consider a laser pulse with intensity $9 \times 10^{20}\,\mathrm{W/cm^2}$ and abrupt plasma-to-vacuum transition.

20% increase of the proton cutoff energy with respect to the case of normal incidence. Around the optimal incidence angle for achieving maximum proton energy, there is a pseudo-plateau between approximately $20^\circ$ and $35^\circ$ where the cutoff energy varies within 5%. Increasing the incidence angle over $45^\circ$ is observed to have a detrimental effect on the acceleration of protons resulting in cutoff energies smaller compared to the case of normal incidence.

The right panel of Figure 9 shows that around the optimal incidence angle, the number of protons accelerated from the target is also enhanced in addition to the increase in proton cutoff energy. For example, around $10\,\mathrm{MeV}$, the incident angle that results in the highest proton cutoff energy also corresponds to the highest number of protons produced near this reference energy.

### 4.3 Impact of target parameters

**Target thickness**

In this set of simulations, we performed a scan over the target thickness by conducting full-scale 3-D PIC simulations. Simulations using a range of target thicknesses revealed that, in the presence of optimal laser contrast and sharp plasma-to-vacuum transition, very thin targets (thicknesses $\leq 2\,\mu\mathrm{m}$) must be used. Only with these very thin targets can proton spectra extending beyond $15\,\mathrm{MeV}$ be achieved (see the left panel of Figure 10 which shows the maximum proton energy versus time for different target thicknesses in simulations employing a laser pulse with intensity on target $I_0 = 9 \times 10^{20}\,\mathrm{W/cm^2}$). This finding requires a detailed evaluation of the laser temporal profile. In the presence of non-optimal contrasts and targets with these thicknesses, there is a concrete risk of disrupting the rear surface of the target by generating a plasma on this surface before the laser pulse reaches its maximum intensity on the front surface. This will deteriorate the performance of TNSA and lead to lower proton energies than those expected from simulations.

We notice that, even under ideal conditions and with thin targets, at this intensity, the proton cutoff energy will be $\sim 17\,\mathrm{MeV}$. As a consequence, the range of energies in which we are interested ($14.5$–$15.5\,\mathrm{MeV}$) will fall very close to the cutoff energy of the proton spectrum. This will make the whole scheme potentially susceptible to experimental fluctuations. It will also reduce the amount of charge available (see the right panel of Figure 10 which shows the proton spectrum at saturation and indicates that only $\sim 10^8$ protons are accelerated to energies of $(15.0 \pm 0.5)\,\mathrm{MeV}$). In the experiments, the thinner the target used, the harder it is to operate the tape target system at high repetition rates. Therefore, there is a trade off here between decreasing the target thickness to enhance the maximum proton energy achievable and keeping the target above a minimum threshold

which allows operation at high enough repetition rate and, thus, the desired throughput for cell irradiation.

**$H^+$ contaminant layer density**

In the TNSA scheme, the strong electrostatic fields resulting from the charge separation at the back surface of the target accelerate positive ions. These ions can include protons (H+), heavier ions from the target material itself (e.g., aluminium ions from an aluminium target), or impurity ions present in the target material or introduced by contaminants. The energies and composition of the accelerated ion beam depend on various factors which may include the composition, density, and thickness of the contaminant layer present on the back surface of the target.

Like on most materials subject to non-ideal vacuum conditions, a surface contaminant layer consisting of hydrocabons and water will form on the tape-like metallic targets that are used in experiments of TNSA. In the simulations presented here, we modelled the contaminants as a single-component layer of hydrogen ions as we mainly explored the acceleration of protons. Due to their highest charge-to-mass ratio, protons are favoured in the acceleration processes. The cloud of protons that are accelerated away from the target screens the accelerating electric field generated by the escaping electrons for all the other heavier ion species.

The thickness of the contaminant layer in our model is severely constrained by the spatial resolution in the longitudinal direction, even though in reality the hydrocarbons form a thinner layer. The $H^+$ ions were inserted on the back of the target inside a thin layer with a thickness of two times the longitudinal size of a grid cell, corresponding to approximately $31.8\,\mathrm{nm}$. The density of the hydrogen layer was chosen as $2 \times 10^{21}\,\mathrm{cm}^{-3}$ so that the integrated density in the longitudinal direction is closer to the range of values found in practice. The other target and laser parameters in the model used here are given in Table 2.

A sharp ion density gradient at the back surface of the target is crucial for effective ion acceleration. Thus, we explored the effect of varying the density of the contaminant layer present on the back of the aluminium target through a series of full-scale 3-D PIC simulations. Figure 11 shows that both the proton cut-off energy and the energy spectrum are influenced by the density of the hydrogen layer. Higher hydrogen densities are associated with the production of faster protons from TNSA. The simulations showed the transverse size of the sheath field at the back of the target to be smaller for higher densities of the hydrogen layer compared to the case of lower densities. As a result, the density of the electrons that are accelerated away from the target may be higher in the case of a denser layer of surface contaminants. In this case, a stronger sheath field may be established and thus, protons could reach higher maximum energies. However, a less dense contaminant layer is seen to enhance the proton flux at intermediate energies of the full spectrum. Thus, a lower density of the hydrocarbon contaminant layer on the back of the target is found to be optimal for LhARA in order to enhance the proton flux around intermediate proton energies. In this case, the proton cut-off energy could be increased for the LhARA proton source by suitable choices of other target and laser parameters as described previously in this report.

Furthermore, we note based on Figure 12 that the density of the hydrogen layer has an observable effect on the angular distribution with which protons are accelerated from the target. For the lowest density of the contaminant layer that we tested, the majority of the protons move away from the target in a cone of approximately $5^\circ$ (half-angle). As the layer of hydrogen on the back of the target becomes denser, we observe significantly more protons being accelerated from the target at larger angles up to $10^\circ$ (half-angle) and even beyond. In the case of the most dense hydrogen layer we explored, a significant proportion of the protons which correspond to the low energy part of the spectrum is produced at a half-angle larger than $5^\circ$.

The disadvantage of varying the contaminant layer density is that such a procedure is not easily achievable in an experimental setup. Typically, heating of the target or ablation by a secondary laser may be performed prior to experiments to eliminate the hydrogen contaminants as much as possible, when more efficient acceleration of heavier ions is desired. Nonetheless, the set of PIC simulations described here suggests that the density of

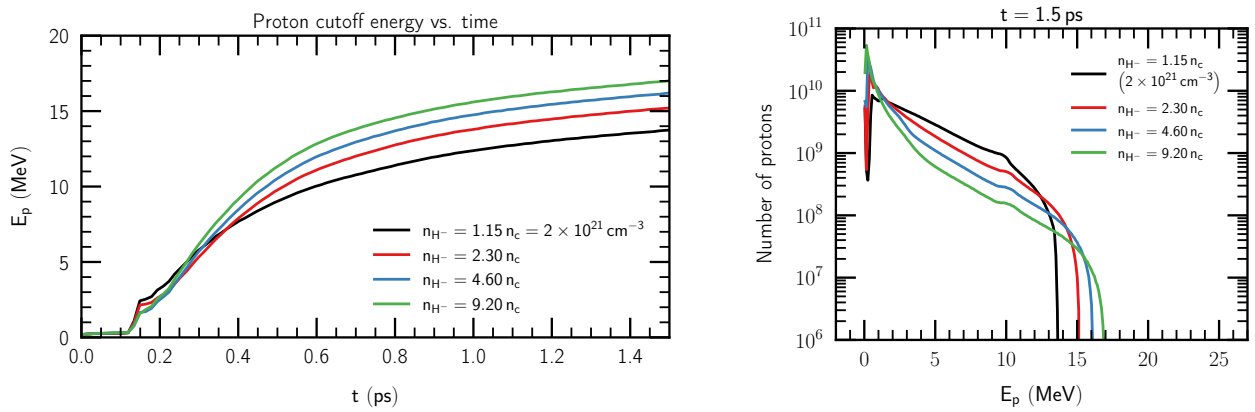


Figure 11: The proton cut-off energy (left) and energy spectrum (right) are influenced by the density of the hydrogen layer deposited on the back of an aluminium target. The local increase in the proton fluxed observed around $10\,\mathrm{MeV}$ in the figure on the right is time-dependent and vanishes at later times in the simulations.

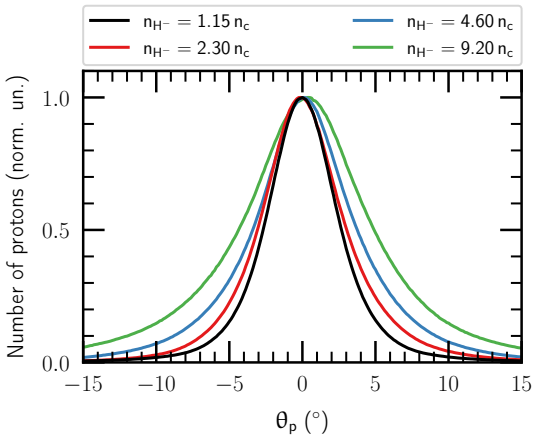


Figure 12: Angular distribution of the protons accelerated from the Al target at energy saturation for four different densities of the hydrogen layer present on the back surface of the target.

the contaminants on the back of the target represents a parameter of interest in order to build better models for TNSA acceleration from tape-like solid targets. A proper choice of the density of the contaminants is needed for quantitative predictions from PIC simulations of TNSA to be correctly compared to data from equivalent experiments.

## 4.4 Impact of preplasma

**Idealised preplasma model**

To explore the presence of a pre-plasma, the front of the target was modelled following a hyperbolic tangent density profile with the parameter $L_g$ determining the pre-plasma scale-length. On the back of the target, a thin layer of $H^+$ ions was inserted to mimic contaminants naturally present on the back surface of solid targets. We carried out simulations considering values of $L_g$ in the range $0.08$–$1\,\mu\mathrm{m}$. Here, $L_g = 0.08\,\mu\mathrm{m}$ corresponds to an almost abrupt plasma-to-vacuum transition and highest laser contrast.

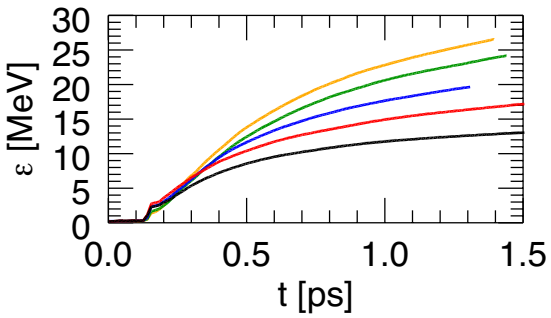


Figure 13: Evolution of the proton cutoff energy for $L_g = 0.08$ (black), 0.3 (red), 0.5 (blue), 0.75 (green) and 1 (yellow) µm and laser $a_0 = 21.60$.

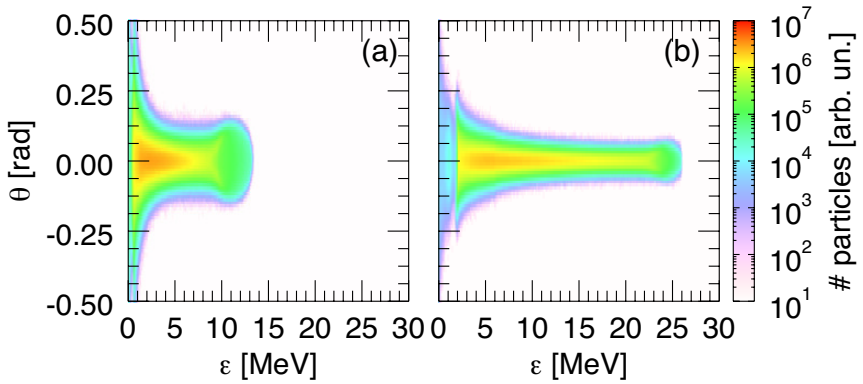


Figure 14: Proton spectrum at saturation for $L_g = 0.08\,\mu\mathrm{m}$ (a) and $1\,\mu\mathrm{m}$ (b). In these simulations $a_0 = 21.60$.

Figure 13 shows the evolution of the proton cutoff energy for different values of $L_g$ and $a_0 = 21.60$. In the case of an almost abrupt plasma-to-vacuum transition, protons reach a maximum energy below $15\,\mathrm{MeV}$. Thus much thinner targets would be necessary to meet LhARA requirements. However, a short scale-length pre-plasma results in increased proton maximum energy beyond $15\,\mathrm{MeV}$. The proton cutoff energy increases approximately linearly with larger pre-plasma scale-length values within the tested range. Increasing the proton cutoff energy well beyond the proton energy desired value of $15\,\mathrm{MeV}$ is preferable because it leads to a higher amount of charge in the selected energy interval of $14.5$–$15.5\,\mathrm{MeV}$. A long-scale-length pre-plasma seems to be also beneficial to achieve proton beams with better spectral properties. Figure 14 shows the angularly resolved proton spectra at saturation for the case of an almost abrupt plasma-to-vacuum transition ($L_g = 0.08\,\mu\mathrm{m}$) and the longest value of $L_g$ modelled. In the latter case, the beam appears to be not only more energetic but also more collimated.

These simulations represented only an initial step to understand the effect of a preplasma in front of the target. The preplasma was modelled in an idealistic way with a very smooth density profile and one scale-length. The bulk of the target is unperturbed. In reality, the formation of a preplasma by either the laser pedestal or a customised prepulse will involve the generation of a shock wave which travels through the target modifying its characteristics. Hydrodynamic simulations were thus necessary to evaluate these effects and provide more detailed information on the preplasma.

**Realistic preplasma model**

In order to improve the model of proton acceleration via TNSA under conditions similar to the preliminary experiments at SCAPA, we used an additional scheme to achieve a more realistic density profile of the preplasma. The expansion of the target due to the laser prepulse was modelled with hydrodynamic simulations as

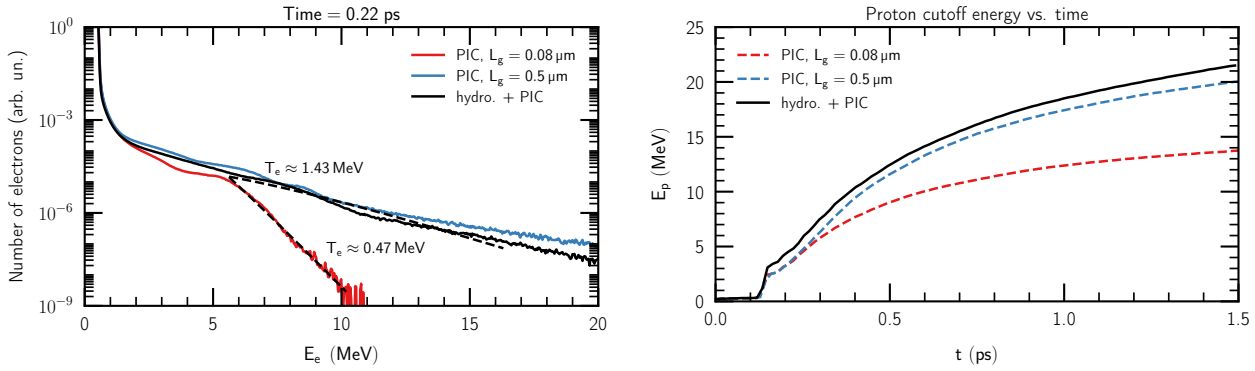


Figure 15: Comparison of the hot electron temperature (left) and proton cutoff energy (right) for three different types of preplasma modelled in front of the solid target from 3-D PIC simulations. An idealised hyperbolic tangent density profile was used to model an abrupt vacuum-to-target transition ($L_g = 0.08\,\mu\mathrm{m}$) and a longer scale-length preplasma ($L_g = 0.5\,\mu\mathrm{m}$). A more realistic model of the preplasma was explored ('hydro. + PIC') by using the target density profile obtained from a hydrodynamic simulation of the interaction of a laser prepulse with the solid target.

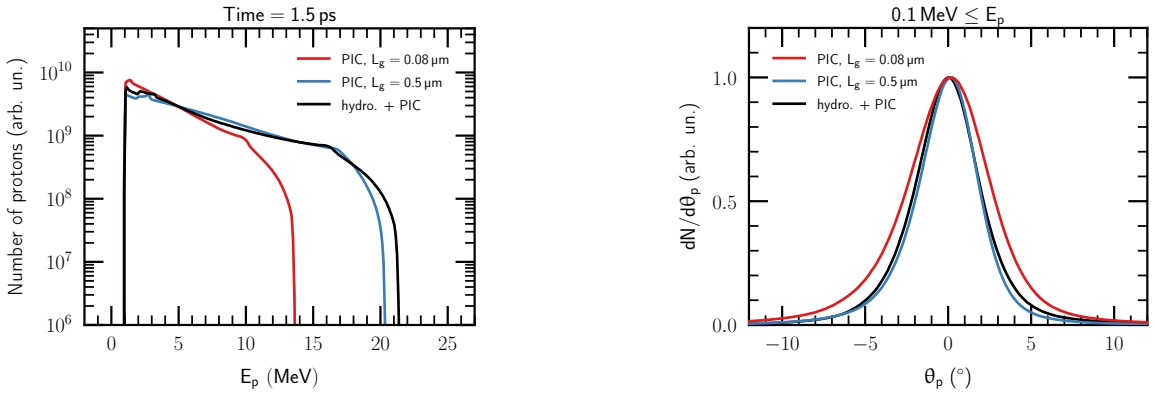


Figure 16: Comparison of the proton energy spectrum (left), and proton production angle (right) for three different types of preplasma modelled in front of the solid target from 3-D PIC simulations (see Figure 15). The local enhancement around $10\,\mathrm{MeV}$ and $17\,\mathrm{MeV}$ are nonphysical artefacts of the simulations.

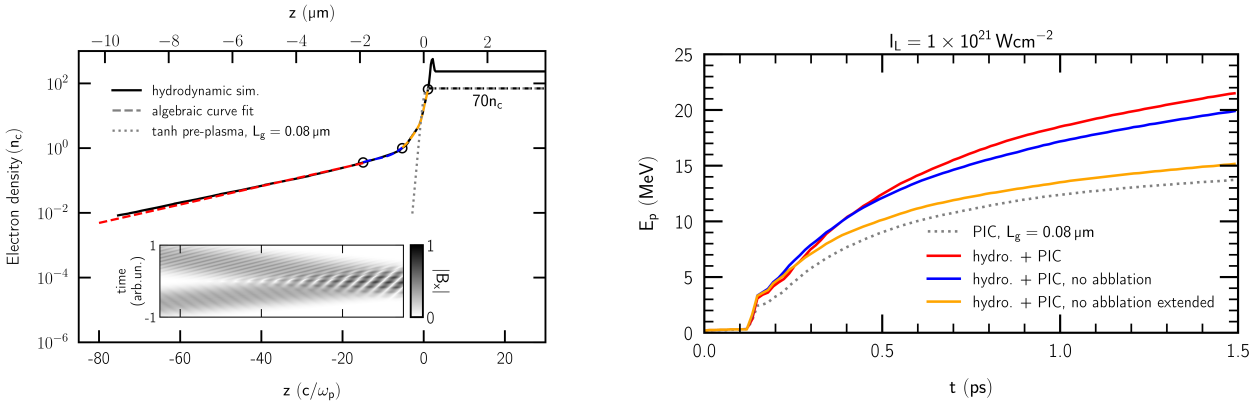


Figure 17: Predicted axial density profile on the front surface of the target resulted from a hydrodynamic simulation of the interaction of the SCAPA laser with an Al target (left panel). The inset shows a theoretical calculation of the extent of the pseudo-standing wave formed at the front of the target by the incident and reflected parts of the laser pulse. The initial target front surface was at $z = 0\,\mu\mathrm{m}$. Evolution of the proton cutoff energy for partial or complete preplasma in front of the bulk of the target (right panel). The boost in the proton cutoff energy increases as more preplasma regions are added to the model further from the front surface of the target into the vacuum: abrupt transition (grey), short scale-length (yellow), absence of abblation region (blue), full preplasma profile (red).

described in section 2. The resulting preplasma density profile was, then, integrated into the PIC simulations to aid the optimisation studies for the final design of the LhARA source. The transition of the target density from vacuum to the bulk of the target in the region of the preplasma can be seen in the right panels of Figures 3 and 4.

We tested the impact of implementing the more realistic preplasma density profile into the PIC simulations by comparing the characteristics of the protons generated via TNSA with those resulting from the idealistic model of the preplasma used previously. Figures 15 and 16 show that the more realistic model of the preplasma results in very similar proton cut-off energy, energy spectrum, and production angles as the ones obtained with the hyperbolic tangent preplasma density at a scale length $L_g = 0.5\,\mu\mathrm{m}$. Consequently, the previous PIC simulations that employed the idealised preplasma model at this particular scale-length can be considered to be a suitable model for the realistic experimental conditions at SCAPA. We observed once more that the presence of the preplasma in front of the bulk of the target enhances the proton cutoff energy significantly compared to an almost abrupt plasma-to-vacuum transition. However, we notice that different preplasma density profiles can lead to similar proton cutoff energies. This can be explained by the very similar number and energy spectra of hot electrons produced when the laser interacts with the preplasma as seen on the left panel of Figure 15.

Figures 15 and 16 summarise the results of 3-D PIC simulations for which we considered a $6\,\mu\mathrm{m}$-thick target and laser intensity $I_0 = 9.97 \times 10^{20}\,\mathrm{W/cm^2}$ ($a_0 = 21.60$). Under these conditions and in combination with the model of the more realistic preplasma based on the laser contrast curve measured at SCAPA, we notice that the proton cutoff energy is $\sim 21\,\mathrm{MeV}$. As a consequence, the range of energies in which we are interested ($14.5$–$15.5\,\mathrm{MeV}$) falls within the pseudo-thermal part of the spectrum and away from the rapid fall near the cutoff energy.

The existence of two preplasma density profiles with different scale-lengths and shapes that result in similar enhancement of the proton cutoff energy indicates that the characteristics of the preplasma can be further optimised. Thus, we continued the campaign of PIC simulations with an attempt to find the optimal preplasma density profile and explore its characteristics.

As a first step, we explored the contribution of different regions of the preplasma to the enhancement of the proton cutoff energy. A laser prepulse leads to the ablation of the front surface of the target which typically results in a plasma density that can be fitted with a double exponential scale. Here, we split the axial target profile predicted by the hydrodynamic simulation in three regions as shown in figure 17 from the target front surface (density $70\,n_c$) to the vacuum: a shorter-scale exponential, a third order polynomial transition region, and a longer-scale exponential. We carried out a set of 3-D PIC simulations for which we considered a $6\,\mu\mathrm{m}$-thick target and laser intensity $I_0 = 9.97 \times 10^{20}\,\mathrm{W/cm^2}$ ($a_0 = 21.60$). We started from the preplasma density profile that corresponds to an almost abrupt plasma-to-vacuum transition (see Figure 17) and we gradually extended the region in front of the target filled by the preplasma by adding one additional region of the preplasma at a time to each subsequent simulation.

The right panel of Figure 17 shows that the longer the preplasma extends in front of the target, the higher the maximum proton energy achieved by TNSA is. However, it was reported before that a saturation regime exists where very long preplasma scale lengths do not lead to an additional increase in the cutoff energy [22, 44]. For example, longer density gradients were found to drive laser filamentation, resulting in significantly lower overall energy coupling [45].

Firstly, Figure 17 indicates that a short-scale preplasma leads to a proton cutoff energy comparable to the almost abrupt plasma-to-vacuum transition. Secondly, a comparatively short ($\sim 1\,\mu\mathrm{m}$) exponential preplasma section with longer scale length is observed to increase the cutoff energy achievable significantly, approximately from $15\,\mathrm{MeV}$ to $20\,\mathrm{MeV}$. Lastly, extending the preplasma even further into the vacuum by a long exponential region with a similarly long scale length provides a marginal increase in the proton cutoff energy of about $1\,\mathrm{MeV}$. Therefore, we found that the region of the preplasma that contributes the most in enhancing the maximum achievable proton energy from TNSA in the presence of a preplasma compared to no preplasma is the $1\,\mu\mathrm{m}$–$2\,\mu\mathrm{m}$-long section that sits in front of the critical density surface. Thus, this region of the preplasma has a density just below the critical density.

A potential explanation for this is that the region of the preplasma that results in the largest proton-energy enhancement factor is also the region where a standing wave is created by the incident and reflected parts of the laser pulse. The inset in the left panel of Figure 17 shows a theoretical calculation of the pseudo-standing wave that is being formed in front of the target. The calculation shows the result of adding the incident part of the laser pulse with the part that is reflected at the critical density surface and which is also slightly redshifted by the propagation of the critical density surface. We notice that the location of the strongest nodes of the transverse magnetic field are exactly within the region of the preplasma that results in the largest proton energy enhancement factor. It has been argued before that electrons can undergo stochastic motion and be accelerated in the subcritical region of the preplasma before they propagate through the target and out of the back surface [23, 46], yielding higher absorption rates and hotter electrons in the presence of an extended preplasma compared to a shorter-scale-length preplasma. Furthermore, at similar laser intensities, the hot electrons were previously shown to be accelerated in the field of a standing electromagnetic wave with the combination of the background plasma channel field [23, 41]. Thus, the largest contribution to the enhancement factor in the proton cutoff energy could be a result of the presence of the preplasma in the region where the standing wave is formed in front of the critical density plane in addition to the preplasma having relatively high but, at the same time, sub-critical density.

In principle, extending the near-critical part of the preplasma further away from the target would not enhance the proton cutoff energy any more if the preplasma was extended beyond the region where the standing wave is formed. In addition, we expect the heating mechanism based on the standing wave to be dependent on the laser pulse duration. For shorter laser pulses, the standing wave pattern is expected to become more transient and the energy coupling to hot electrons to become less efficient. However, other effects may start to become significant and provide additional contributions to boosting the maximum proton energies achievable. One possible

candidate is the self-focusing of the laser pulse while it propagates through the sub-critical preplasma. In order to explore such effects, we carried out a first attempt to find an optimal density profile for the preplasma in the case of normal incidence of the laser onto the target.

**Optimal preplasma density profile (at normal laser incidence)**

In order to explore other preplasma density profiles that could potentially increase the maximum proton energies achievable with the SCAPA laser we carried out a parameter scan using 2-D PIC simulations. The scan was guided by a genetic algorithm so that it could find the 'optimal' preplasma density profiles which results in the highest proton cutoff energy achievable with a specific set of laser and target parameters. From the class of genetic algorithms, we used the 'differential evolution' (DE) scheme, which is specifically designed to deal with continuous variables. The DE algorithm is aimed at optimising an objective function by testing many different candidate hypotheses creating a 'population' that reproduces and evolves over many generations. The algorithm that we implemented follows the canonical structure of differential evolution [47]. The particular set of hyperparameters, as well as the mutation, crossover, and selection procedures were selected according to a previous report of using DE for optimising laser-plasma interaction for proton acceleration [48].

In this work, each population was composed of 60 separate 2-D PIC simulations, each defined by a corresponding set of six 'genes' (i.e. six parameters that define a particular preplasma density profile in front of the bulk of the target). As a typical starting point for DE algorithms, the size of the population was chosen to be ten times as large as the number of free parameters. We let the algorithm evolve for 30 generations, resulting in a total of 1800 2-D PIC simulations. Each simulation ran for approximately six minutes on ARCHER2 with four simulations running concurrently. Together with the time required to compute the objective function, transfer data from and to the computing cluster, and to advance the generations, the total execution time of the optimisation scan was less than two days. Hence, by using 2-D simulations we explored orders of magnitude more target configurations than would be possible with three dimensions.

To optimise the acceleration of protons, we chose the objective function to be the maximum proton energy at the end of the simulation after the saturation of the proton cutoff energy. Thus, as the generations evolved, the preplasma profiles that resulted in the largest proton cutoff energies were passed over, while less efficient preplasma conditions were disregarded by the algorithm. The simulations have a spatial resolution of $0.125\,(c/\omega_0)$) with 64 electron, 144 hydrogen, and 16 aluminium macroparticles per cell. The macroparticles are initialised with thermal temperatures of $10\,\mathrm{keV}$ and the simulation time is $800\,\mathrm{fs}$ with a time step of $0.037\,\mathrm{fs}$.

The initial population, shown in the left panel of Figure 18, consisted of sixty different preplasma density profiles chosen randomly by generating the parameters that define each profile from uniform distributions within the allowed ranges. As a result, the first generation represents a good sample over the parameter space as it contains preplasma density profiles characterised by comparatively short, intermediate, and long scale-lengths.

The right panel of figure 18 shows the members of the last (30th) generation which resulted from running the DE algorithm. We notice that all the members of the last generation have converged such that the corresponding preplasma density profiles have similar shapes. Firstly, the preplasma extends up to $\sim 13\,\mu\mathrm{m}$ in front of the bulk of the target which was the maximum allowed length that we set up at the beginning of the optimisation procedure. This indicates that higher proton cutoff energies are favoured by preplasmas with long scale-lengths. At the same time, most of the 'optimal' preplasma profiles we found consist of a foam-like layer with an approximately constant density of $\sim 1\,n_c$ that extends over 60–80% of the total length of the preplasma. In addition to the foam-like region, the 'optimal' preplasma density profiles exhibit a short scale-length section where the density drops from $70\,n_c$ to $<10\,n_c$ in less than $1\,\mu\mathrm{m}$, and an intermediate scale-length section extending over $\sim 4\,\mu\mathrm{m}$.

Figure 19 shows how the proton cutoff energy extracted from the simulations improve with each generation.

In the initial generation, the best-performing preplasma density profile results in a cutoff energy of approximately $65\,\mathrm{MeV}$. The following generations improve upon this result, eventually reaching nearly $110\,\mathrm{MeV}$ in the 30th generation, with most of this improvement coming from the first ten or so generations. The last ten generations only improve the cutoff energy by a negligible amount, which is part of our rationale for ending the optimisation procedure after 30 generations. Since we carried out PIC simulations in two dimensions for the optimisation procedure, we expect the proton cutoff energy to be overestimated by a factor in the range 2–3 [34].

To validate that the preplasma density profile found by the differential evolution algorithm can push the proton spectrum to higher energies, we carried out a full-scale 3-D PIC simulation for identical preplasma conditions. Figure 21 confirms that significantly higher proton energies can be generated in the presence of a foam-like near-critical-density preplasma. In particular, the 3-D simulation indicates that proton energies of up to $45\,\mathrm{MeV}$ can be obtained without changing the other laser and target parameters. A comparison of the spectra from the 2-D and 3-D simulations shows that in two dimensions the proton energy was overestimated by a factor of approximately $1.6$ in the case of the preplasma density profile obtained with the hydrodynamic simulation and $2.2$ in the case of the optimal preplasma profile found in the optimisation procedure compared to the prediction using three dimensions. Furthermore, we noticed that in the presence of a comparatively long length-scale preplasma, the accelerating sheath field decays slower in time and, thus, protons reach energy saturation at later times in simulations compared to the cases of no or shorter scale-length preplasma. In addition to the enhancement of the cutoff energy, the optimal preplasma we found results in a proton emission opening angle approximately half of the angle found for the case of a shorter scale-length preplasma. At higher energies above $10\,\mathrm{MeV}$, all the protons are produced within a half angle of approximately $100\,\mathrm{mrad}$.

The uniform near-critical-density layer in front of the target is a distinct feature of the 'optimal' preplasma density profiles that we found by the optimisation procedure. The classically slightly overdense layer at the start of the preplasma becomes relativistically transparent, allowing the laser pulse to pass. This first phase of the interaction is reminiscent of studies where ion acceleration is enhanced by relativistic transparency [49–51]. While passing through the near-critical density region, the laser transfers significant energy to electrons. In addition, we notice that the relatively long scale-length preplasma results in focusing of the laser pulse, thus, leading to stronger electromagnetic fields when the pulse hits the bulk of the target. Figure 22 shows that the laser spot is focused transversely due to the propagation through the foam-like layer of the preplasma as indicated by 2-D PIC simulations.

A more elaborate picture of the effect that the preplasma scale length has on the propagation of the laser before it reaches the target is shown in Figure 23. The two cases highlighted in Figure 23 correspond to the case of an optimal preplasma density profile and a more realistic one which were simulated in three dimensions. The laser propagation through the preplasma in combination with the kinetic energy density of the electrons originating in the preplasma region indicate part of the mechanism that leads to higher proton cutoff energy in the case of longer scale-length preplasmas (see Figures 20 and 21). When a near-critical low-gradient long plasma is present in front of the target, the laser penetrates through the underdense plasma, where it undergoes self-focusing and steepening (Figure 23h). When the laser reaches the plasma region where $n_c \leq n_e \leq \langle\gamma\rangle n_c$ ($n_e$ being the electron density, $n_c$ being the critical density and $\langle\gamma\rangle n_c$ the relativistic critical density, where $\langle\gamma\rangle = \sqrt{1 + a_0^2/2}$), it expels electrons forming semi-circular cavities (see Figure 23d) [22, 52, 53]. We notice that these cavities are less well-observable in the case of the more realistic preplasma with a shorter-scale-length preplasma. In the presence of an extended preplasma, a larger number of electrons reach higher energies (Figure 23i,j).

Overall, these results indicate that the enhancement of the proton cutoff energy is due to the interplay between the laser pulse self-focusing, pulse steepening, the stochastic heating of fast electrons, and the potential laser filamentation starting at longer preplasma scale lengths [45]. However, further investigations are needed to fully

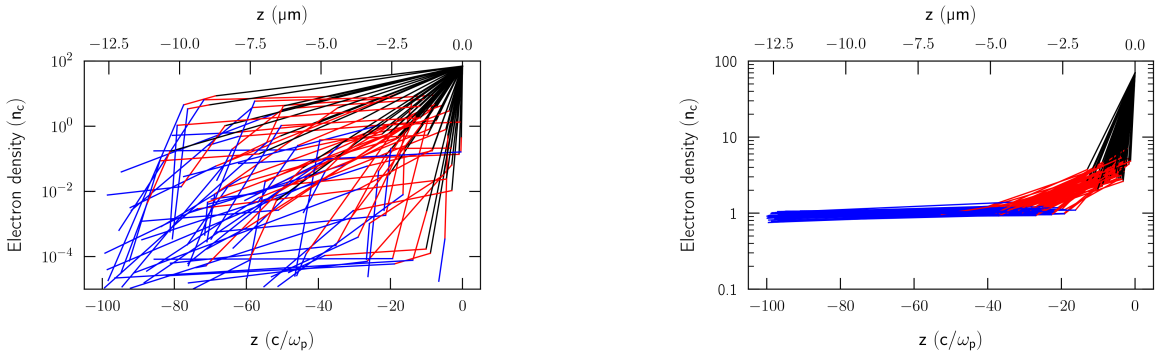


Figure 18: The initial (left) and last (right) generations of preplasma density profiles from the differential evolution optimisation scheme. The profiles in the starting generation were randomly generated. All the density profiles in the last generation exhibit a comparatively long foam-like near-critical density preplasma in front of the bulk of the target.

understand the role of each process in the overall laser-target interaction. Nonetheless, reliable experimental techniques that modify the vacuum-target interface could potentially offer control of these mechanisms and, thus, have strong impact on the effectiveness of accelerating protons beams via TNSA.

Finally, it needs to be mentioned that, in practice, it is challenging to manufacture a high-repetition target that could consist of a solid tape with an added layer of foam on the front surface. However, in principle, a near-critical preplasma with a long scale-length may be obtained by suitably tailoring the strength and timing of one or multiple laser prepulses with respect to the main high-intensity pulse. The work we carried out to find an optimal preplasma density profile is planned to continue by exploring the characteristics of the laser contrast curve that are required to generate in an experiment an optimal preplasma profile from a solid target.

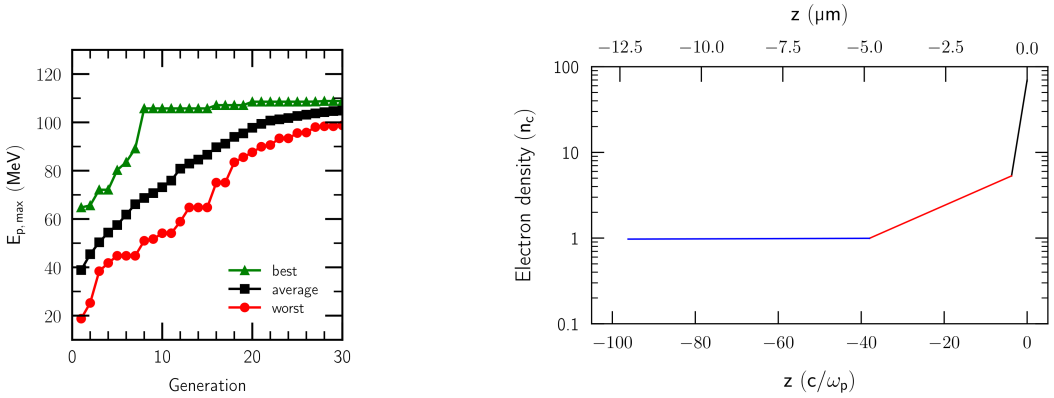


Figure 19: The increase of the maximum, average, and minimum proton cutoff energy from the initial to the last generation (left panel). The best proton cutoff energy increases quickly and then begins to level off with later generations. The cutoff energies were evaluated with 2D PIC simulations which typically overestimate the final ion energy. The 'optimal' density profile in the last generation is shown in the right panel. An approximately critical density region with a very long scale-length in front of the bulk of the target provides the maximum proton cutoff energy.

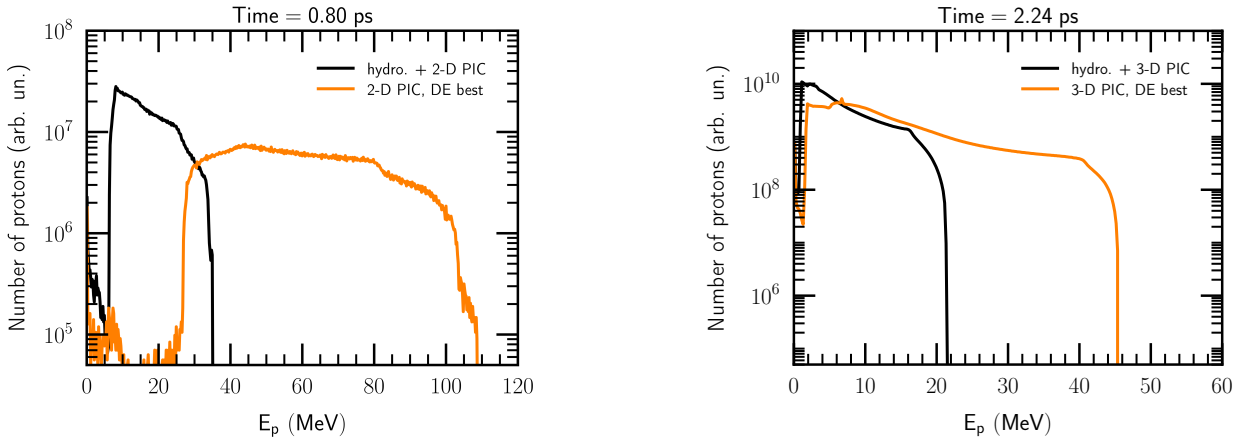


Figure 20: Proton energy spectra at saturation for a model of the preplasma density profile corresponding to the laser contrast measured at SCAPA (black) and the optimal preplasma density profile found by the evolutionary algorithm (orange). Both cases were evaluated with 2-D (left) and 3-D (right) PIC simulations.

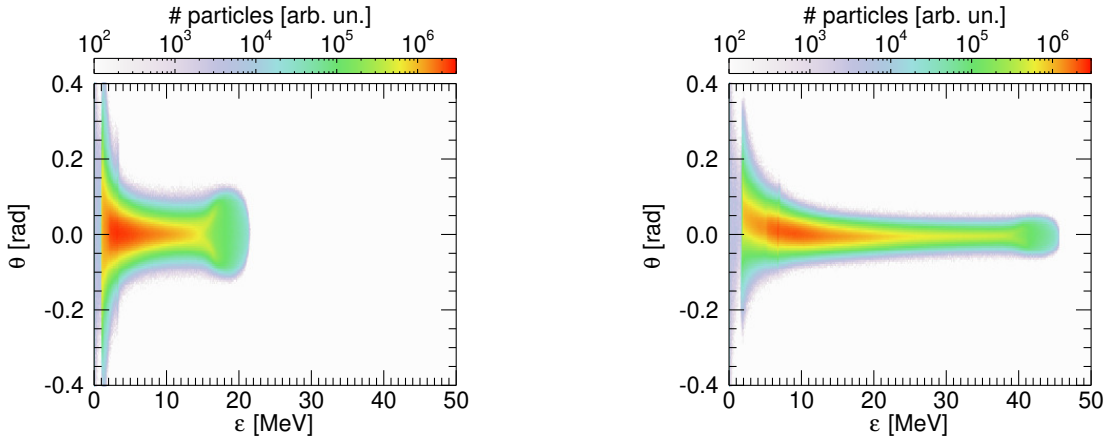


Figure 21: Proton spectrum at saturation for a model of the preplasma density profile corresponding to the laser contrast measured at SCAPA (left) and the optimal preplasma density profile found by the evolutionary algorithm (right). These 3-D PIC simulations considered a target thickness of $6\,\mu\mathrm{m}$ and a laser intensity $I_0 = 9.97 \times 10^{20}\,\mathrm{W/cm^2}$.

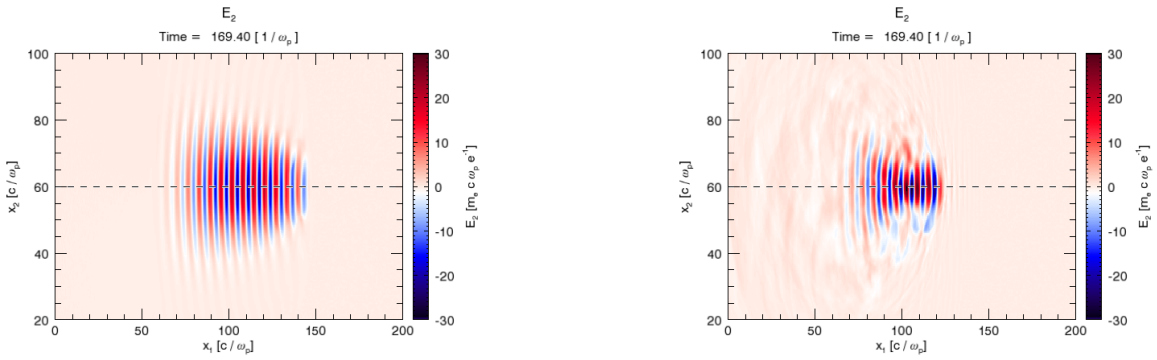


Figure 22: The laser pulse just before it hits the front surface of the bulk of the target for the model of a realistic preplasma from SCAPA (left) and the optimal preplasma found by the differential evolution algorithm (right). The foam-like near-critical density preplamsa leads to the focusing of the laser pulse seen on the right panel and to enhanced acceleration via TNSA. The front surface of the bulk of the target is located at $x_1 = 150\,(c/\omega_p)$.

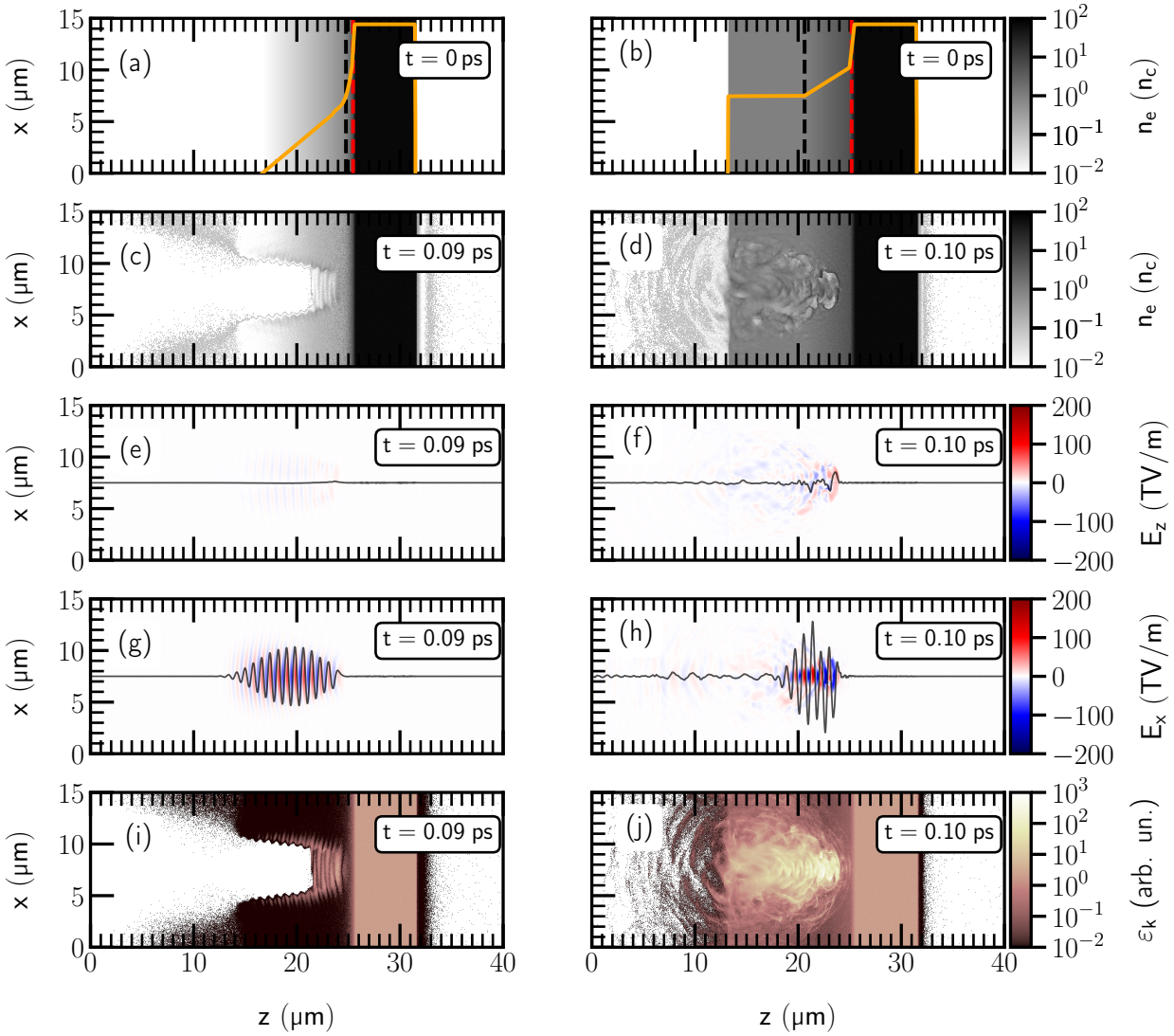


Figure 23: 3-D PIC simulations: (**a, b**) electron density at the start of the simulation, (**c, d**) electron density a short time before the laser reaches the bulk of the target, (**e, f**) longitudinal electric field, (**g, h**) transverse electric field, and (**i, j**) electron kinetic energy density for an $Al^{3+}$ target with a preplasma density profile obtained from a hydrodynamic simulation (left column) and the optimal preplasma conditions found by the 2-D scan using a differential evolution scheme (right column). The black and red dashed lines in (**a, b**) denote the position of the critical density and the relativistic critical density, respectively. The orange lines in (**a, b**) show the density lineout along the propagation axis of the laser. The black solid lines in (**e, f, g, h**) represent the electric field lineout in the middle of the simulation box.

# 5 Baseline for the LhARA proton source

## 5.1 Summary of the key laser and target requirements

The work outlined in this report resulted in a set of predictions regarding the laser and target parameters required to meet the nominal proton beam characteristics required for the LhARA proton source. Here, we summarise the main conclusions that should guide future experimental campaigns and the development of the LhARA source.

Firstly, simulations using a range of target thicknesses revealed that, in the presence of ultra-high laser contrast and sharp plasma-to-vacuum transition, very thin targets (thicknesses $\leq 2\,\mu\mathrm{m}$ in the case of aluminium) must be used. Only with these very thin targets can proton spectra extending beyond $15\,\mathrm{MeV}$ be achieved for laser intensities close to $9 \times 10^{20}\,\mathrm{W/cm^2}$.

Secondly, under the exact conditions of target thickness and ultra-high laser contrast, the parameter scan over laser intensity suggests a more powerful laser must be considered. In particular, to extend the proton spectrum beyond $20\,\mathrm{MeV}$ and accelerate sufficient protons to energies of $(15.0 \pm 0.5)\,\mathrm{MeV}$, it is required to use laser intensities $\gg 1 \times 10^{21}\,\mathrm{W/cm^2}$. However, an optimally controlled contrast with sufficiently thick targets could pre-expand the front surface of the target leading to preplasma formation but leaving the rear surface of the target intact.

In additional parameter scans, the angle of incidence of the laser onto the target and the density of the contaminant layer on the back surface of the target were both observed to play a role in the energy spectrum of the accelerated protons. We found an optimal angle of incidence of $\sim 28^\circ$ that enhances the proton cutoff energy by approximately $20\,\%$ compared to the case of normal incidence in 2-D simulations. Angles of incidence higher than $40^\circ$ seem to be detrimental to proton acceleration via TNSA. An additional increase of the cutoff energy of protons was observed when the density of the hydrogen layer at the back of the target was increased. However, such a change was accompanied by lower proton numbers in the exponential part of the energy spectrum. Even though the density of the contaminants on surface of the target is not a parameter that can be easily controlled in an experimental setting, its value must be carefully chosen in PIC simulations if a quantitative comparison between experiments and simulations is desired.

The presence of a preplasma was confirmed by simulations to enable more efficient electron heating mechanisms. In turn, this translates into higher proton energies. We have also considered the possibility that a prepulse be used to generate the preplasma in front of the target in a more controlled way. Simulations modelling an idealised preplasma in front of the target seem to indicate that proton spectra extending beyond $20\,\mathrm{MeV}$ can be achieved with targets $>2\,\mu\mathrm{m}$ thick and laser intensities $\lesssim 1 \times 10^{21}\,\mathrm{W/cm^2}$. We found the proton cutoff energy to increase approximately linearly with larger preplasma scale-length values within the range that we tested. In addition to pushing the energy spectrum to higher values, a long-scale-length preplasma seems to be beneficial to achieve proton beams with better spectral properties (smaller opening angle at the target).

Furthermore, we improved our simulation model by including a more realistic preplasma density extracted from separate hydrodynamic simulations of the pre-expansion of the target before the arrival of the main laser pulse. For this, we used a preliminary measurement of the laser contrast curve at SCAPA. We found that the more realistic target conditions result in a proton energy spectrum very similar to the one obtained previously by using the idealised preplasma model with the largest scale-length that we tested. The observation of two different preplasma density profiles that resulted in similar enhancement of the proton cutoff energy motivated us to attempt to further evaluate whether the preplasma density distribution could be further optimised.

As a result, we carried out a parameter scan using 2-D PIC simulations and a differential evolution algorithm to find an optimal preplasma density profile for a fixed set of laser and target parameters. The objective was to maximise the proton cutoff energy by splitting the preplasma into three sections and varying the scale-length

and longitudinal extent of each of the sections. A total of 1800 different preplasma density profiles were simulated and the optimisation procedure converged towards a set of density distributions with very similar aspect. We found that the proton cutoff energy is maximised within the constraints we used when the main laser pulse is incident on a foam-like near-critical density layer with a thickness of several micrometres before the higher density part of the preplasma and the bulk of the target. Even though a foam-like preplasma is difficult to be achieved experimentally on a solid target built for high-repetition shots, we plan to investigate whether similar density profiles can be produced by tailoring the laser contrast curve with the use of one or potentially more laser prepulses. On SCAPA, the generation of a controlled prepulse with a variable delay with respect to the main pulse is already available.

In addition to the 2-D scan of the preplasma density profiles, we carried out a full-scale 3-D PIC simulation to evaluate the proton energies achievable in the case of using the optimal density profile that resulted from the 2-D scan. We found the 2-D simulation to have overestimated the proton cutoff energy by a factor between 1.6 and 2.2 compared to the prediction using three dimensions. Hence, the 3-D simulation indicates that the preplasma density profile that resulted from the optimisation study pushes the proton energy spectrum to energies up to $45\,\mathrm{MeV}$. However, the number of protons with energy close to $15\,\mathrm{MeV}$ is of a similar magnitude in both the presence of an optimal preplasma and of a more realistic one. Nonetheless, the production half-opening angle is reduced compared to the case of a shorter length-scale preplasma. Under optimal preplasma conditions, the protons with energy in the range $(15.0 \pm 0.5)\,\mathrm{MeV}$ are emitted from the target with an RMS divergence of $19\,\mathrm{mrad}$ and within a cone with a half opening angle of $99\,\mathrm{mrad}$.

## 5.2 Predicted proton production rate and spectra

As a result of the multiple scans we performed over a wide parameter space, we highlight in this section the most important characteristics of the protons produced by the laser-driven source that we modelled. Table 3 provides a set of parameters for the proton source as obtained with high-fidelity 3-D PIC simulations. We focus in particular on two scenarios. Firstly, the 'realistic' conditions referred to in Table 3 include the nominal laser and target parameters listed in Table 2 and are based on a model of the preplasma density profile obtained with the hydrodynamic simulation as described in section 2. Secondly, the source parameters we listed in Table 3 under 'optimal' conditions correspond to the case of an ideal preplasma density profile present on the front surface of the target based on the work we described in the previous sections of this report.

In addition to the enhancement of the proton cutoff energy due to the presence of an optimal preplasma, increasing the laser intensity and using a thinner target may push the cutoff of the energy spectrum and, hence the proton number within the energy range of interest for LhARA, to even higher values. This would require laser intensities higher than the threshold of $10^{21}\,\mathrm{W/cm^2}$ and very thin targets (thicknesses $\leq 2\,\mu\mathrm{m}$). In the presence of non-optimal contrasts and targets with these thicknesses, there is a concrete risk of disrupting the rear surface of the target by generating a plasma on this surface before the laser pulse reaches its maximum intensity on the front surface. This may lead to lower proton energies than those expected from simulation. It must also be mentioned that Table 3 is based on simulations of a laser hitting the target at normal incidence as modelling oblique incidence in three dimensions exceeded the computational resources available to us. Thus, a further enhancement of the cutoff energies and proton fluxes presented in Table 3 are expected if the laser is incident on the target at an optimal angle of incidence, as shown by 2-D simulations.

We considered the reference energy interval $(15.0 \pm 0.5)\,\mathrm{MeV}$ to account for potential rotations in the longitudinal phase space of the proton beam done by RF cavities envisioned as part of the LhARA beamline which could finally deliver a higher proton flux within the nominal energy range of $15\,\mathrm{MeV} \pm 2\,\%$. Capturing protons from the source within an energy band larger than $1\,\mathrm{MeV}$ before the passage through the RF cavities is one potential technique that could increase the number of protons with nominal energy delivered to the end stations.

Table 3: Summary of the baseline parameters for the LhARA proton source as predicted by high-fidelity hydrodynamic and 3-D kinetic simulations (at normal laser incidence).

| | **Parameter** | **Value** | **Unit** |
|---|---|---|---|
| Realistic conditions | Cutoff energy | 21.5 | MeV |
| | Particle number per pulse ($15.0 \pm 0.5\,\mathrm{MeV}$) | $3.1 \times 10^8$ | |
| | RMS beam divergence ($>1\,\mathrm{MeV}$) | 52 | mrad |
| | RMS beam divergence ($15.0 \pm 0.5\,\mathrm{MeV}$) | 32 | mrad |
| | Max. emission half opening angle ($15.0 \pm 0.5\,\mathrm{MeV}$) | 141 | mrad |
| | Emittance[‡] | 0.133 | mm-mrad |
| Optimal conditions[†] | Cutoff energy | 45.4 | MeV |
| | Particle number per pulse ($15.0 \pm 0.5\,\mathrm{MeV}$) | $4.0 \times 10^8$ | |
| | RMS beam divergence ($>1\,\mathrm{MeV}$) | 33 | mrad |
| | RMS beam divergence ($15.0 \pm 0.5\,\mathrm{MeV}$) | 19 | mrad |
| | Max. emission half opening angle ($15.0 \pm 0.5\,\mathrm{MeV}$) | 99 | mrad |
| | Emittance[‡] | 0.052 | mm-mrad |

[†]Here, optimal conditions refer to the preplasma density profile we found to result in the maximum proton cutoff energy for the nominal laser and target parameters listed in Table 2.

[‡]RMS emittance, $\epsilon_{\mathrm{RMS}} = \sqrt{\langle x^2 \rangle \langle x'^2 \rangle - \langle x \cdot x' \rangle^2}$

Moreover, the simulations outlined in this report indicate that similar numbers of protons are produced with energy within the reference interval both under optimal and more realistic laser and target conditions. We must note that the energy within the laser pulse is one of the main factors that influence the number of protons accelerated from the target per each laser pulse. As we considered a rather conservative value of the laser energy in our simulations, a higher particle number per pulse may be measured in the experiments at SCAPA dedicated to the development of the LhARA source.

Finally, Table 3 includes the half angle of the full emission cone for the protons within the reference energy range. The maximum emission angle dictates the angular acceptance required from the capture system in LhARA to ensure 100% transmission of the protons within the reference energy interval downstream from the source to the rest of the beamlines.

## 6 Modelling of TNSA for heavy ion acceleration on SCAPA

As a first step in studying the effect of the laser and target parameters on the acceleration of carbon ions from a solid target in the context of LhARA, we performed an initial high-fidelity PIC simulation with $C^{6+}$ ions. We chose a set of target and laser parameters that were previously reported in this work to result in protons with comparatively high energies. In principle, the same laser and target parameters are expected to lead to similar electron heating and, thus, to an accelerating sheath with similar strength as in the case of accelerating protons, irrespective of the ion species that constitutes the contaminant layer on the back of the target.

On the one hand, we chose a set of laser and target parameters that are not challenging to achieve experimentally: $6\,\mu\mathrm{m}$-thick Al target, laser intensity $9.97 \times 10^{20}\,\mathrm{W/cm^2}$, realistic preplasma density profile based on the laser contrast curve measured at SCAPA. In principle, the cutoff energy of carbon ions could be pushed to higher values by using ultra-thin targets and preplasma profiles with even longer scale-lengths. On the other hand, the simulation considers the optimal case in which $C^{6+}$ ions are the only species present on the back of the target, thus ensuring maximum acceleration efficiency since there is no other species with a higher charge-to-mass ratio which could screen part of the accelerating field. Thus, the initial simulation we report here represents a good 'close-to-optimal' scenario which provides a preliminary evaluation of the capability of a LhARA-type source to produce ions heavier than the proton.

The p-polarised laser pulse was focused on the target to a spot size $w_0$ of $1.5\,\mu\mathrm{m}$ and had a FWHM pulse duration of $25\,\mathrm{fs}$. The target was modelled as a pre-formed plasma composed of $Al^{3+}$ ions and electrons with density with density $70\,n_c \sim 10^{23}\,\mathrm{cm^{-3}}$ (here $n_c$ is the critical density corresponding to the laser frequency). To include the presence of a preplasma, the density at the front of the target was modelled according to the results of the hydrodynamic simulation described in section 2 and based on the preliminary measurement of the laser contrast curve at SCAPA. On the back of the target, a thin layer of $C^{6+}$ ions was inserted to mimic hydrocarbons naturally present on the back surface of solid targets. However, carbon was considered as the only ion species on the back of the target which models the case of using a target-cleaning technique in an experimental setting to remove other contaminants.

As in the case of proton acceleration, the left panel of Figure 24 shows that the cutoff energy of the carbon ions increases rapidly a short time after the laser hits the target and then reaches saturation at later times. The interval of time required for the cutoff energy to reach saturation is longer than in the case of proton acceleration as expected due to the lower charge-to-mass ratio. As a result, more computational resources may be needed for high-fidelity simulations and parameter scans of carbon acceleration compared to the case of protons. This preliminary simulation indicates that, under the conditions considered here, carbon ions can be accelerated to a maximum energy of approximately $11\,\mathrm{Mev/u}$. The ion cutoff energy was $11.13\,\mathrm{MeV/u}$ at the last time step of the simulation presented here. This result is comparable to the cutoff energy predicted in the case of accelerating protons under similar laser and target conditions (maximum energy $\sim 22\,\mathrm{MeV/u}$ as shown in

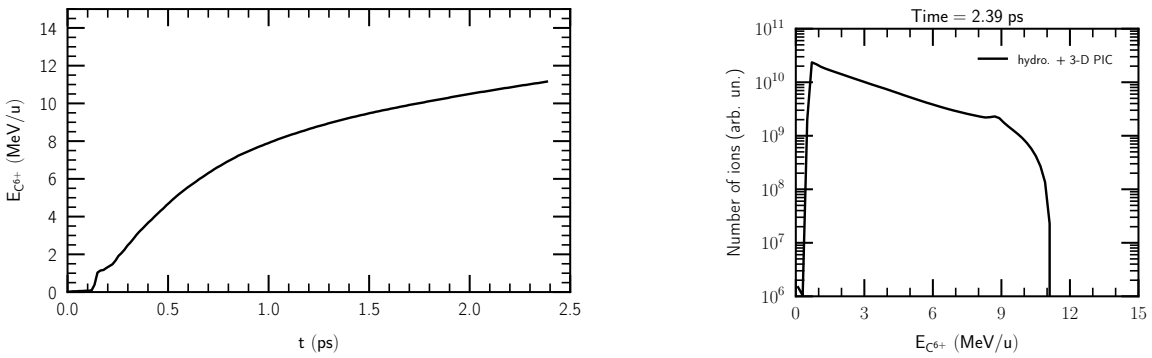


Figure 24: Evolution of the carbon ($C^{6+}$) cutoff energy (left panel). Carbon energy spectrum at saturation for a 6 µm-thick Al target (right panel). This simulation considers a laser pulse with intensity $9.97 \times 10^{20}\,\mathrm{W/cm^2}$ and a realistic preplasma density profile based on a preliminary laser contrast curve measured at SCAPA. The layer of contaminants on the back of the target consisted only of carbon ions.

Figure 20. However, Figure 24 shows that the cutoff energy has not completely reached saturation despite of the relatively long interval of time captured by the simulation.

In addition to the evolution of the cutoff energy, Figure 24 shows the energy spectrum of the carbon ions at the last time step of the simulation. The spectrum exhibits the main characteristics typical to TNSA: broad-band pseudo-thermal spectrum with a sharp cutoff. As an indication of the ion flux, the number of $C^6+$ ions produced within the energy range $(4.0 \pm 0.5)\,\mathrm{MeV/u}$ is $2.6 \times 10^8$ (248 pC). The correlation between the ion energy and the angle of emission from the target is shown in Figure 25. The ions with energy $>1\,\mathrm{MeV/u}$ propagate away from the target in a cone with an RMS half opening angle of $20\,\mathrm{mrad}$.

We note that this simulation represents only an initial step to find the optimal conditions for the acceleration of carbon ions by the source envisioned for LhARA. In reality, other ion species are present on the back of the target which screen part of the accelerating field and lead to lower ion energies. Further simulations are needed to evaluate how strongly the energy spectrum of carbon is affected by the presence of other contaminants on the surface of the target.

As a preliminary investigation, Figure 26 shows how the presence of hydrogen ions in addition to carbon ions on the back surface of the target leads to a lower cutoff energy for the heavier ion species due to screening of the accelerating field caused by the protons being accelerated faster from the target. The ion energy spectra in Figure 26 were obtained by considering an equal density of hydrogen and carbon ions on the back of the target. Under these conditions, the cutoff energy of the carbon ions is approximately three times lower than the maximum energy of carbon achieved in an equivalent simulation with no other contaminant ion species beside carbon on the back of the target. The preliminary simulation suggests that the presence of the hydrogen ions in addition to the carbon layer may lead to the acceleration of a higher number of carbon ions from the target. Approximately $7.3 \times 10^8$ (705 pC) $C^6+$ ions are predicted by the simulation within the energy range $(4.0 \pm 0.5)\,\mathrm{MeV/u}$ with a cutoff energy of $4.5\,\mathrm{MeV}$.

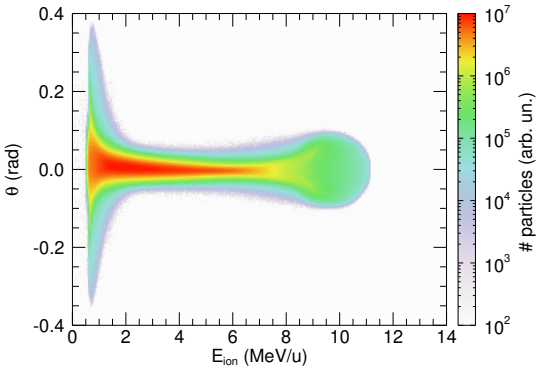


Figure 25: Carbon ($C^{6+}$) spectrum (emission angle, $\theta$, vs. kinetic energy, $E_{\text{ion}}$) at energy saturation ($6\,\mu\text{m}$-thick Al target, laser intensity $9.97\times10^{20}\,\text{W/cm}^2$, realistic preplasma density profile based on the laser contrast curve measured at SCAPA. The layer of contaminants on the back of the target consisted only of carbon ions.

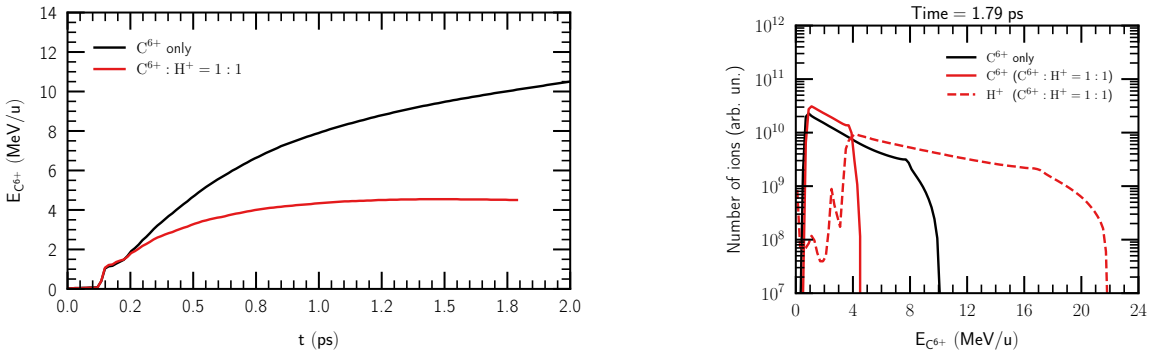


Figure 26: Evolution of the carbon ($C^{6+}$) cutoff energy (left panel). Carbon and proton energy spectrum at $1.8\,\text{ps}$ for a $6\,\mu\text{m}$-thick Al target (right panel). This simulation considers a laser pulse with intensity $9.97\times10^{20}\,\text{W/cm}^2$ and a realistic preplasma density profile based on a preliminary laser contrast curve measured at SCAPA. The layer of contaminants on the back of the target consisted only of carbon ions or of an equal density mixture of carbon and hydrogen ions $\left(C^{6+}:H^{+}=1:1\right)$.

# 7 Conclusions

In summary, we carried out a comprehensive series of high-fidelity hydrodynamic and kinetic (particle-in-cell) simulations to predict a set of optimised proton source parameters for 300+ TW laser systems. We investigated the impact of several laser and target parameters on the acceleration of protons and carbon ions via TNSA from a solid target. The results we presented in this report predict lower or upper thresholds for the source parameters that will ensure the acceleration of protons with the energy and flux required for LhARA. In the presence of optimal laser contrast and sharp plasma-to-vacuum transition, very thin targets ($<2\,\mu\mathrm{m}$) and laser intensities $\gg 10^{21}\,\mathrm{W/cm^2}$ are required to extend the proton spectrum beyond $20\,\mathrm{MeV}$ and accelerate sufficient protons to energies of $(15.0 \pm 0.5)\,\mathrm{MeV}$.

In addition, we identified general trends and specific conditions which result in optimal acceleration of protons. For example, an incidence angle close to $30^\circ$ was predicted to enhance the proton cutoff energy by approximately $20\,\%$. Furthermore, the proper modelling of the laser contrast and density profile of the target emerged as important factors which play a significant role in obtaining realistic energy spectra of the protons accelerated via TNSA. Our results showed that a preplasma with a several-micrometers-long scale-length and near-critical density can strongly enhance proton acceleration even with the use of not-so-thin tape targets. The formation of a preplasma with an optimal density profile by the use of a laser prepulse represents an alternative to using a higher-intensity main laser pulse or thinner targets to extend the proton cutoff energy and the particle flux beyond those required for LhARA.

The work presented in this report demonstrates the importance of controlling and measuring the preplasma density profile for creating optimal conditions for proton and ion acceleration from solid targets via TNSA. In a scenario when the highest available laser intensity is used in combination with the thinnest target that can be run on the tape-drive system, controlling the preplasma represents one of the few remaining approaches to further increase the maximum achievable energy and the number of the protons accelerated from the target. Thus, a key outcome of this report is the importance of developing new methods to measure and control the preplasma for solid targets that can be run at high repetition rates. While the generation of a controlled prepulse with a variable delay with respect to the main pulse is already available at SCAPA, a campaign explicitly aiming to establish new methods to measure and control the preplasma would be one next step in optimising the production of protons from the LhARA source. In particular, a dedicated programme is required to develop techniques for LhARA that would enable quantitative measurements of the preplasma.

As a preliminary exploration using high-fidelity PIC simulations of heavy-ion acceleration for LhARA, we found that carbon ions are predicted to reach energies of up to $11\,\mathrm{MeV/u}$ from the source under conditions very similar to the optimal scenario for proton acceleration. Nonetheless, further work is planned to optimise the laser and target parameters specifically for heavy ion acceleration. In addition, we plan to continue the campaign of hydrodynamic simulations to explore how the laser contrast or a prepulse can be used to generate a preplasma with a density profile close to the optimal one. Meanwhile, the predictions from the simulations outlined in this report have already started to guide the baseline experiments at SCAPA. The data from the experimental campaigns is necessary to validate the optimal conditions found by our programme of hydrodynamics and PIC simulations. Once validated, the results outlined in this report will be integrated into the final laser and target specifications for LhARA.

## References


[1] The LhARA consortium, "The Laser-hybrid Accelerator for Radiobiological Applications," Tech. Rep. CCAP-TN-01, The Centre for the Clinical Application of Particles, Imperial College London, 2020. https://ccap.hep.ph.ic.ac.uk/trac/raw-attachment/wiki/Communication/Notes/CCAP-TN-01.pdf.

[2] S. M. Wiggins, M. Boyd, E. Brunetti, *et al.*, "Application programmes at the Scottish Centre for the Application of Plasma-based Accelerators (SCAPA)," in *Relativistic Plasma Waves and Particle Beams as Coherent and Incoherent Radiation Sources III*, D. A. Jaroszynski and M. Hur, eds., vol. 11036, p. 110360T, International Society for Optics and Photonics. SPIE, 2019. doi:10.1117/12.2520717.

[3] T.-S. Dascalu, *Study of non-neutral electron plasma lenses for focusing laser-driven ion beams*. Phd thesis, Imperial College London, May, 2023. doi:10.25560/107391.

[4] L. A. Gizzi, "Laser-Driven Sources of High Energy Particles and Radiation," in *Laser-Driven Sources of High Energy Particles and Radiation*, pp. 1–24. Springer, 2019. doi:10.1007/978-3-030-25850-4, doi:10.1007/978-3-030-25850-4.

[5] A. J. Mackinnon, Y. Sentoku, P. K. Patel, *et al.*, "Enhancement of Proton Acceleration by Hot-Electron Recirculation in Thin Foils Irradiated by Ultraintense Laser Pulses," *Phys. Rev. Lett.* **88** (05, 2002) 215006, doi:10.1103/PhysRevLett.88.215006.

[6] R. A. Snavely, M. H. Key, S. P. Hatchett, *et al.*, "Intense High-Energy Proton Beams from Petawatt-Laser Irradiation of Solids," *Phys. Rev. Lett.* **85** (10, 2000) 2945–2948, doi:10.1103/PhysRevLett.85.2945.

[7] P. McKenna, K. W. D. Ledingham, J. M. Yang, *et al.*, "Characterization of proton and heavier ion acceleration in ultrahigh-intensity laser interactions with heated target foils," *Phys. Rev. E* **70** (9, 2004) 036405, doi:10.1103/PhysRevE.70.036405.

[8] M. Nishiuchi, A. Fukumi, H. Daido, *et al.*, "The laser proton acceleration in the strong charge separation regime," *Physics Letters A* **357** (2006), no. 4, 339–344, doi:10.1016/j.physleta.2006.04.053.

[9] D. C. Carroll, O. Tresca, R. Prasad, *et al.*, "Carbon ion acceleration from thin foil targets irradiated by ultrahigh-contrast, ultraintense laser pulses," *New Journal of Physics* **12** (4, 2010) 045020, doi:10.1088/1367-2630/12/4/045020.

[10] F. Nürnberg, M. Schollmeier, E. Brambrink, *et al.*, "Radiochromic film imaging spectroscopy of laser-accelerated proton beams," *Review of Scientific Instruments* **80** (2009), no. 3, 033301, doi:10.1063/1.3086424.

[11] M. Roth and M. Schollmeier, "Ion Acceleration—Target Normal Sheath Acceleration," *CERN Yellow Reports* (2016) Vol 1 (2016): Proceedings of the 2014 CAS–CERN Accelerator School: Plasma Wake Acceleration, doi:10.5170/CERN-2016-001.231.

[12] J. Fuchs, T. E. Cowan, P. Audebert, *et al.*, "Spatial Uniformity of Laser-Accelerated Ultrahigh-Current MeV Electron Propagation in Metals and Insulators," *Phys. Rev. Lett.* **91** (12, 2003) 255002, doi:10.1103/PhysRevLett.91.255002.

[13] H. Daido, M. Nishiuchi, and A. S. Pirozhkov, "Review of laser-driven ion sources and their applications," *Reports on Progress in Physics* **75** (4, 2012) 056401, doi:10.1088/0034-4885/75/5/056401.

[14] Y. Sentoku, V. Y. Bychenkov, K. Flippo, *et al.*, "High-energy ion generation in interaction. of short laser pulse with high-density plasma," *Applied Physics B 2002 74:3* **74** (2, 2014) 207–215, doi:10.1007/S003400200796.

[15] E. L. Clark, K. Krushelnick, M. Zepf, *et al.*, "Energetic Heavy-Ion and Proton Generation from Ultraintense Laser-Plasma Interactions with Solids," *Phys. Rev. Lett.* **85** (8, 2000) 1654–1657, doi:10.1103/PhysRevLett.85.1654.

[16] S. Keppler, N. Elkina, G. A. Becker, *et al.*, "Intensity scaling limitations of laser-driven proton acceleration in the TNSA-regime," *Phys. Rev. Res.* **4** (Jan, 2022) 013065, doi:10.1103/PhysRevResearch.4.013065.

[17] M. N. ul Haq, H. Ahmed, T. Sokollik, *et al.*, "Parametric scalings of laser driven protons using a high repetition rate tape drive target system," *Nuclear Instruments and Methods in Physics Research Section A: Accelerators, Spectrometers, Detectors and Associated Equipment* **909** (2018) 164–167, doi:https://doi.org/10.1016/j.nima.2018.02.108. 3rd European Advanced Accelerator Concepts workshop (EAAC2017).

[18] J. Fuchs, P. Antici, E. d'Humières, *et al.*, "Laser-driven proton scaling laws and new paths towards energy increase," *Nature Physics* **2** (Jan., 2006) 48–54, doi:10.1038/nphys199.

[19] N. P. Dover, M. Nishiuchi, H. Sakaki, *et al.*, "Effect of Small Focus on Electron Heating and Proton Acceleration in Ultrarelativistic Laser-Solid Interactions," *Phys. Rev. Lett.* **124** (Feb, 2020) 084802, doi:10.1103/PhysRevLett.124.084802.

[20] T. Ziegler, C. Bernert, S. Bock, *et al.*, "Proton beam quality enhancement by spectral phase control of a PW-class laser system," *Scientific Reports* **11** (2021) 7338, doi:10.1038/s41598-021-86547-x.

[21] T. Ceccotti, A. Lévy, H. Popescu, *et al.*, "Proton Acceleration with High-Intensity Ultrahigh-Contrast Laser Pulses," *Phys. Rev. Lett.* **99** (Oct, 2007) 185002, doi:10.1103/PhysRevLett.99.185002.

[22] L. A. Gizzi, E. Boella, L. Labate, *et al.*, "Enhanced laser-driven proton acceleration via improved fast electron heating in a controlled pre-plasma," *Scientific Reports* **11** (July, 2021) 13728, doi:10.1038/s41598-021-93011-3.

[23] L. Chopineau, A. Leblanc, G. Blaclard, *et al.*, "Identification of Coupling Mechanisms between Ultraintense Laser Light and Dense Plasmas," *Phys. Rev. X* **9** (Mar, 2019) 011050, doi:10.1103/PhysRevX.9.011050.

[24] P. McKenna, D. Carroll, O. Lundh, *et al.*, "Effects of front surface plasma expansion on proton acceleration in ultraintense laser irradiation of foil targets," *Laser and Particle Beams* **26** (2008), no. 4, 591–596, doi:10.1017/S0263034608000657.

[25] B. M. Hegelich, B. J. Albright, J. Cobble, *et al.*, "Laser acceleration of quasi-monoenergetic MeV ion beams," *Nature* **439** (Jan., 2006) 441–444, doi:10.1038/nature04400.

[26] P. Sommer, J. Metzkes-Ng, F.-E. Brack, *et al.*, "Laser-ablation-based ion source characterization and manipulation for laser-driven ion acceleration," *Plasma Physics and Controlled Fusion* **60** (mar, 2018) 054002, doi:10.1088/1361-6587/aab21e.

[27] K. Zeil, J. Metzkes, T. Kluge, *et al.*, "Robust energy enhancement of ultrashort pulse laser accelerated protons from reduced mass targets," *Plasma Physics and Controlled Fusion* **56** (2014) 084004, doi:10.1088/0741-3335/56/8/084004.

[28] H. Kiriyama, Y. Miyasaka, A. Kon, *et al.*, "Enhancement of pre-pulse and picosecond pedestal contrast of the petawatt J-KAREN-P laser," *High Power Laser Science and Engineering* **9** (2021) e62, doi:10.1017/hpl.2021.51.

[29] B. Fryxell, K. Olson, and P. Ricker, "FLASH: An Adaptive Mesh Hydrodynamics Code for Modeling Astrophysical Thermonuclear Flashes," *The Astrophysical Journal Supplement Series* **131** (2000) 273–334, doi:10.1086/317361.

[30] J. M. Dawson, "Particle simulation of plasmas," *Rev. Mod. Phys.* **55** (Apr, 1983) 403–447, doi:10.1103/RevModPhys.55.403.

[31] R. A. Fonseca, L. O. Silva, F. S. Tsung, *et al.*, "OSIRIS: A Three-Dimensional, Fully Relativistic Particle in Cell Code for Modeling Plasma Based Accelerators," in *Computational Science — ICCS 2002*, P. M. A. Sloot, A. G. Hoekstra, C. J. K. Tan, and J. J. Dongarra, eds., pp. 342–351. Springer Berlin Heidelberg, Berlin, Heidelberg, 2002. doi:10.1007/3-540-47789-6_36.

[32] ARCHER2–UK National Supercomputing Service. `https://www.archer2.ac.uk/`, 2024. Accessed: May 2024.

[33] SuperMUC-NG. `https://doku.lrz.de/supermuc-ng-10745965.html`, 2024. Accessed: May 2024.

[34] A. Sgattoni, P. Londrillo, A. Macchi, and M. Passoni, "Laser ion acceleration using a solid target coupled with a low-density layer," *Phys. Rev. E* **85** (Mar, 2012) 036405, doi:10.1103/PhysRevE.85.036405.

[35] J. Babaei, L. A. Gizzi, P. Londrillo, *et al.*, "Rise time of proton cut-off energy in 2D and 3D PIC simulations," *Physics of Plasmas* **24** (04, 2017) 043106, doi:10.1063/1.4979901.

[36] D. J. Stark, L. Yin, B. J. Albright, and F. Guo, "Effects of dimensionality on kinetic simulations of laser-ion acceleration in the transparency regime," *Physics of Plasmas* **24** (05, 2017) 053103, doi:10.1063/1.4982741.

[37] P. J. Bilbao, "Towards a better understanding of Target Normal Sheath Acceleration experiments at the Laser Light Ion beam-line (L3IA) aided by an exhaustive Parameter Scan," Master's thesis, Lancaster University, June, 2020.

[38] "OSIRIS Reference Guide." `https://osiris-code.github.io/osiris/reference/zpulse`. Accessed: May 2024.

[39] J. Schreiber, F. Bell, F. Grüner, *et al.*, "Analytical Model for Ion Acceleration by High-Intensity Laser Pulses," *Phys. Rev. Lett.* **97** (Jul, 2006) 045005, doi:10.1103/PhysRevLett.97.045005.

[40] C. M. Brenner, P. McKenna, and D. Neely, "Modelling the effect of laser focal spot size on sheath-accelerated protons in intense laser–foil interactions," *Plasma Physics and Controlled Fusion* **56** (jul, 2014) 084003, doi:10.1088/0741-3335/56/8/084003.

[41] R. Babjak and J. Psikal, "The role of standing wave in the generation of hot electrons by femtosecond laser beams incident on dense ionized target," *Physics of Plasmas* **28** (02, 2021) 023107, doi:10.1063/5.0031555.

[42] J. May, J. Tonge, F. Fiuza, *et al.*, "Mechanism of generating fast electrons by an intense laser at a steep overdense interface," *Phys. Rev. E* **84** (Aug, 2011) 025401, doi:10.1103/PhysRevE.84.025401.

[43] T. Morita, T. Z. Esirkepov, S. V. Bulanov, *et al.*, "Tunable High-Energy Ion Source via Oblique Laser Pulse Incident on a Double-Layer Target," *Phys. Rev. Lett.* **100** (Apr, 2008) 145001, doi:10.1103/PhysRevLett.100.145001.

[44] Y. Sentoku, V. Y. Bychenkov, K. Flippo, *et al.*, "High-energy ion generation in interaction. of short laser pulse with high-density plasma," *Applied Physics B* **74** (Mar., 2002) 207–215, doi:10.1007/s003400200796.

[45] R. J. Gray, D. C. Carroll, X. H. Yuan, *et al.*, "Laser pulse propagation and enhanced energy coupling to fast electrons in dense plasma gradients," *New Journal of Physics* **16** (nov, 2014) 113075, doi:10.1088/1367-2630/16/11/113075.

[46] R. Nuter, L. Gremillet, P. Combis, *et al.*, "Influence of a preplasma on electron heating and proton acceleration in ultraintense laser-foil interaction," *Journal of Applied Physics* **104** (11, 2008) 103307, doi:10.1063/1.3028274.

[47] R. Storn and K. Price, "Differential Evolution – A Simple and Efficient Heuristic for global Optimization over Continuous Spaces," *Journal of Global Optimization* **11** (Dec., 1997) 341–359, doi:10.1023/A:1008202821328.

[48] J. R. Smith, C. Orban, J. T. Morrison, *et al.*, "Optimizing laser–plasma interactions for ion acceleration using particle-in-cell simulations and evolutionary algorithms," *New Journal of Physics* **22** (oct, 2020) 103067, doi:10.1088/1367-2630/abbfce.

[49] F. Wagner, O. Deppert, C. Brabetz, *et al.*, "Maximum Proton Energy above 85 MeV from the Relativistic Interaction of Laser Pulses with Micrometer Thick $CH_2$ Targets," *Phys. Rev. Lett.* **116** (May, 2016) 205002, doi:10.1103/PhysRevLett.116.205002.

[50] P. L. Poole, L. Obst, G. E. Cochran, *et al.*, "Laser-driven ion acceleration via target normal sheath acceleration in the relativistic transparency regime," *New Journal of Physics* **20** (jan, 2018) 013019, doi:10.1088/1367-2630/aa9d47.

[51] A. Higginson, R. J. Gray, M. King, *et al.*, "Near-100 MeV protons via a laser-driven transparency-enhanced hybrid acceleration scheme," *Nature Communications* **9** (Feb., 2018) 724, doi:10.1038/s41467-018-03063-9.

[52] S. C. Wilks, W. L. Kruer, M. Tabak, and A. B. Langdon, "Absorption of ultra-intense laser pulses," *Phys. Rev. Lett.* **69** (Aug, 1992) 1383–1386, doi:10.1103/PhysRevLett.69.1383.

[53] F. Tsung, S. Y. Tochitsky, D. J. Haberberger, *et al.*, "CO2 Laser acceleration of forward directed MeV proton beams in a gas target at critical plasma density," *Journal of Plasma Physics* **78** (2012), no. 4, 373–382, doi:10.1017/S0022377812000189.